Materials Today Communications 57 (2026) 116428

Contents lists available at ScienceDirect

Materials Today Communications

journal homepage: www.elsevier.com/locate/mtcomm

# Agro-waste valorization of beet peel extract as a sustainable corrosion inhibitor for tinplate in simulated black olive brine: Integrated experimental investigation and molecular-level insights

Amel Serhane [a], Yamina Boudinar [b], Hakim Bensabra [a], Noura Naili [b,c], Amina Benaissa [d,e], Sihem Boufas [f], Abdul Ahad [g], Hyun-Jo Ahn [h], Byong-Hun Jeon [h,*], Yacine Benguerba [i,*]

[a] Laboratory of Applied Energetics and Materials (LEAM), University of Jijel, B.P. 98 Ouled Aïssa Jijel, 18000, Algeria
[b] Laboratory of Anticorrosion Materials, Environment, and Structure, 20 Août 1955 University, P.O. Box 26, Skikda 21000, Algeria
[c] Unité de Recherche de Chimie de l'Environnement et Moléculaire Structurale, Université Constantine 1 (Mentouri), Constantine 25000, Algeria
[d] Department of Chemistry, Faculty of Science, 20 Août 1955 University, P.O. Box 26, Skikda 21000, Algeria
[e] Laboratory of Génie Chimique et Environnement de Skikda, Département of Process Engineering, Faculty of Technology, 20 Août 1955 University, P.O. Box 26, Skikda 21000, Algeria
[f] Department of Technology, Faculty of Technology, 20 August 1955 University, P.O. Box 26, El-Hadaik Road, Skikda 21000, Algeria
[g] Department of Pharmaceutics, College of Pharmacy, King Saud University, P.O. Box 2457, Riyadh 11451, Saudi Arabia
[h] Department of Earth Resources and Environmental Engineering, Hanyang University, 222 Wangsimni-ro, Seongdong-gu, Seoul 04763, Republic of Korea
[i] Laboratoire de Biopharmacie et Pharmacotechnie (LPBT), Ferhat Abbas Sétif 1 University, Sétif 19000, Algeria

ARTICLE INFO

*Keywords:*
Beet peel extract (BPE)
DFT
Electrochemical impedance spectroscopy (EIS)
Green corrosion inhibitor
Simulated black olive brine (SBOB)
Tinplate

ABSTRACT

The development of sustainable corrosion protection strategies based on renewable resources is increasingly important for reducing the environmental impact of conventional corrosion inhibitors. In this study, beet peel extract (BPE), an abundant agro-industrial byproduct, was investigated as a bio-based corrosion inhibitor for tinplate exposed to simulated black olive brine. The inhibition performance and underlying protection mechanism were systematically assessed using gravimetric measurements, open-circuit potential monitoring, potentiodynamic polarization, electrochemical impedance spectroscopy (EIS), scanning electron microscopy coupled with energy-dispersive X-ray spectroscopy (SEM-EDX), Fourier transform infrared spectroscopy (FTIR), and liquid chromatography mass spectrometry (LC-MS). Experimental investigations were complemented by density functional theory (DFT) calculations and molecular dynamics (MD) simulations to provide molecular-level insights into the adsorption process. BPE exhibited a pronounced concentration-dependent inhibition effect, reaching maximum inhibition efficiencies of 99.38% from EIS measurements and 94.8% from gravimetric analysis at 300 mg $L^{-1}$ . Electrochemical measurements indicated a substantial increase in charge-transfer resistance accompanied by a decrease in corrosion current density, consistent with the formation of an adsorbed protective layer on the tinplate surface. SEM-EDX and FTIR analyses further supported the formation of an inhibitor-derived surface film involving oxygen-containing and polyphenolic constituents identified by LC-MS. The Langmuir isotherm satisfactorily described the adsorption behavior, while the corresponding thermodynamic parameters indicated a spontaneous adsorption process involving both physical and chemical contributions.

## 1. Introduction

Tinplate is a low-carbon steel sheet coated on both sides with a thin electrolytically deposited tin layer [1,2]. Owing to its mechanical strength, formability, corrosion resistance, and compatibility with food-processing operations, it remains one of the most widely used metallic materials for food packaging. Nevertheless, the protective tin layer is not completely impermeable. Local defects, pores, scratches, or discontinuities in the coating can expose the underlying steel substrate to the packaged medium. At the same time, chemical interactions between the metal surface and aggressive food constituents may promote tin dissolution and localized corrosion [3]. Oxygen ingress through

* Corresponding authors.
*E-mail addresses:* bhjeon@hanyang.ac.kr (B.-H. Jeon), yacinebenguerba@univ-setif.dz (Y. Benguerba).

https://doi.org/10.1016/j.mtcomm.2026.116428
Received 20 July 2026; Received in revised form 2 October 2026; Accepted 18 October 2026
Available online 19 October 2026
2352-4928/© 2026 The Authors. Published by Elsevier Ltd. This is an open access article under the CC BY-NC-ND license (http://creativecommons.org/licenses/by-nc-nd/4.0/).

coating defects can further accelerate degradation of the underlying steel and modify the nature of the surface oxide layer. Protective organic lacquers are therefore commonly applied to the internal surfaces of cans, with coating selection depending strongly on food composition and acidity. Despite the technological and economic importance of tinplate, its corrosion and corrosion-inhibition behavior in mildly acidic or near-neutral food-simulating media remains less extensively investigated than that of conventional carbon steel in strongly acidic environments [4,5].

Increasing environmental and regulatory concerns associated with conventional synthetic corrosion inhibitors have stimulated considerable interest in renewable, biodegradable, and low-toxicity alternatives. Plant-derived materials, including crude extracts, essential oils, and isolated phytochemicals, have consequently emerged as promising sources of corrosion inhibitors. Several plant products, such as *Lawsonia* extract [6], *Hibiscus sabdariffa* extract [7], *Garcinia kola* extract [8], and fenugreek extract [9], have shown substantial inhibition efficiencies for metallic substrates, particularly carbon steel exposed to acidic media. Their protective action is generally associated with the adsorption of organic constituents containing aromatic rings, heteroatoms, hydroxyl groups, carbonyl groups, and conjugated π-electron systems, which can interact with metallic surfaces and reduce the kinetics of anodic metal dissolution and/or cathodic reactions.

Plant extracts are chemically complex multicomponent systems, and their inhibition performance depends on the composition of the extract, the nature of the metallic substrate, the corrosive medium, and the adsorption behavior of the major phytochemical constituents. Polyphenols, flavonoids, tannins, and related oxygen-containing compounds are frequently regarded as important contributors because they can adsorb on metallic interfaces and promote the formation of protective organic films. Such adsorption is often analyzed using classical adsorption models, including the Langmuir isotherm [10]. However, for multicomponent natural extracts, deviations from ideal adsorption behavior may arise from competitive adsorption, lateral interactions between adsorbates, and differences in the surface affinity of individual constituents. Consequently, mechanistic interpretation requires the combined use of electrochemical, surface-analytical, and molecular-level approaches rather than reliance on a single experimental descriptor.

Recent studies increasingly combine gravimetric measurements, potentiodynamic polarization, electrochemical impedance spectroscopy, surface characterization, and computational chemistry to obtain a more comprehensive description of plant-derived corrosion inhibitors. For example, *Datura stramonium* extract has been investigated for Zn in HCl using electrochemical and surface characterization approaches. In contrast, Eucalyptus leaf extract has been evaluated for Al in HCl using weight-loss, polarization, impedance, and complementary theoretical analyses. Such studies demonstrate the value of integrating experimental and computational methods. Nevertheless, these systems involve substrates and highly acidic environments that differ considerably from tinplate exposed to food-related chloride media. Therefore, their mechanistic conclusions cannot be transferred directly to a heterogeneous tin-coated steel surface operating under the mildly acidic conditions encountered in food packaging.

In parallel with the search for environmentally acceptable corrosion inhibitors, the valorization of agro-industrial residues has become an important component of sustainable materials research. Beet processing generates substantial quantities of peel waste that may contain phenolic and other oxygen-rich organic compounds with antioxidant and metal-interacting properties. Converting this residue into a functional corrosion inhibitor, therefore, provides a dual environmental benefit by contributing simultaneously to waste valorization and sustainable corrosion control. In the present work, beet peel extract (BPE) is investigated as a bio-based inhibitor for tinplate exposed to simulated black olive brine (SBOB), a chloride-containing mildly acidic medium selected to represent conditions relevant to canned-food storage.

The novelty of the present study lies primarily in the specific combination of inhibitor, substrate, corrosive environment, and molecular-modeling strategy. To the best of our knowledge, BPE has not previously been evaluated as a corrosion inhibitor for tinplate in SBOB. Importantly, tinplate should not be treated as equivalent to bare carbon steel because it is intrinsically heterogeneous, consisting of a steel substrate covered by a thin tin layer together with tin-oxide species. During service, local defects or degradation of the coating may expose Fe-rich regions while intact areas remain dominated by Sn/$SnO_2$. Consequently, adsorption on a single generic metallic surface cannot fully represent the interfacial behavior of inhibitor molecules on tinplate.

To address this heterogeneity, the experimental investigation was coupled with a multi-surface computational approach. Density Functional Theory (DFT) calculations were used to characterize the structural and electronic properties of the major constituents identified in BPE, while Molecular Dynamics (MD) simulations were performed comparatively on Fe(110), Sn(001), and $SnO_2$(001) surfaces. This strategy makes it possible to examine differences in adsorption affinity and molecular orientation between exposed iron regions and the intact tin/tin-oxide coating, thereby providing a more realistic molecular-level description of the tinplate/inhibitor interface [11–17].

Experimentally, the inhibition performance of BPE was evaluated using complementary gravimetric and electrochemical techniques, including weight-loss measurements, open-circuit potential monitoring, potentiodynamic polarization (PDP), and electrochemical impedance spectroscopy (EIS). Surface and chemical characterization was carried out using attenuated total reflectance Fourier-transform infrared spectroscopy (ATR-FTIR), scanning electron microscopy coupled with energy-dispersive X-ray spectroscopy (SEM–EDX), and liquid chromatography–mass spectrometry (LC–MS). The integration of these techniques was intended to relate inhibition efficiency and electrochemical response to surface-film formation and to the chemical composition of the extract.

Accordingly, the objectives of this study were to: **(i)** evaluate the corrosion-inhibition efficiency of BPE for tinplate in SBOB and determine the concentration giving the highest protection under the investigated conditions; **(ii)** clarify the influence of BPE on the anodic and cathodic corrosion processes using polarization and impedance measurements; **(iii)** characterize the surface and chemical changes associated with inhibitor adsorption; and **(iv)** correlate the experimental observations with molecular reactivity and adsorption behavior of the principal BPE constituents on Fe(110), Sn(001), and $SnO_2$(001). Through this integrated experimental–computational framework, the study aims to provide a more realistic understanding of bio-based corrosion inhibition on heterogeneous tinplate surfaces and to support the valorization of beet-processing waste as a potentially sustainable corrosion-protection resource.

## 2. Materials and methods

### 2.1. Materials and specimen preparation

Tinplate, a material widely used in the food industry for the production of metal packaging, was selected as the metallic substrate in this study. Its chemical composition, determined by X-ray fluorescence spectroscopy (XRF), is presented in Table 1. The tinplate consists of low-carbon steel coated with a thin electrolytically deposited tin layer approximately 2 μm thick, which provides essential protection against corrosion and enhances its suitability for food contact packaging applications by limiting metal dissolution and surface degradation.

**Table 1**
Chemical composition of tinplate.

| Element | Fe | Sn | Mn | Cu | Cr |
|---|---|---|---|---|---|
| Wt (%) | 98.55 | 1.04 | 0.311 | 0.063 | 0.033 |

The electrodes were shaped into rectangular pieces, and a shielded conductive wire was carefully soldered to each one to ensure a stable electrical connection. They were then covered with insulating tape, leaving only an exposed active area of 1 $cm^2$ to be used during the electrochemical measurements.

### 2.2. Corrosive test media

This solution was prepared to simulate the storage environment of Meradja black olives, a product from the industrial zone of Tlemcen. To formulate the medium, 41 g of sodium chloride (NaCl) was dissolved in one liter of distilled water at 20 °C. The pH was then carefully adjusted to 4 using acetic acid, while maintaining continuous stirring to ensure full and uniform homogenization (Simulated black olive brine SBOB).

### 2.3. Extraction of plant material

The beetroot peels used in this work were first rinsed thoroughly with distilled water to remove any adhering dust or residues. They were then spread out and allowed to air dry in a clean and well-ventilated place until completely dry. Once dried, the peels were finely milled using an electric grinder (Robot-coupe type) to obtain a smooth and uniform powder. The resulting powder was then subjected to a gentle maceration process in a hydro-alcoholic solvent composed of 70% ethanol and 30% distilled water. The mixture was left to stand for 72 h at room temperature, allowing the solvent to extract the main bioactive constituents of the plant material, particularly polyphenols and antioxidant compounds. Following maceration, the mixture was passed through filter paper to remove any remaining solid particles and recover the liquid extract. This extract was subsequently concentrated using reduced-pressure evaporation at 40 °C, a gentle process that helps maintain the stability of the bioactive molecules. The resulting viscous concentrate was then stored properly until it was needed for the experimental procedures.

### 2.4. Weight loss measurement

Prior to immersion, the tinplate specimens were degreased, dried thoroughly, and accurately weighed using an analytical balance (precision ±0.1mg). Weight loss tests were conducted by completely immersing the coupons in 100mL of SBOB solution at ambient temperature (20 ± 1°C) for 72h, both in the absence and presence of various concentrations of BPE (100, 200, 300, and 400mg·$L^{-1}$). All gravimetric measurements were carried out in triplicate ($n$ = 3) using independently prepared specimens, and the data are reported as mean $\pm$ standard deviation. Upon retrieval after 72h, the specimens were chemically cleaned in accordance with the ASTM G1 standard to selectively remove corrosion products without attacking the metallic substrate, rinsed with distilled water, dried, and immediately reweighed to determine the mass loss ($\Delta W$). The resulting gravimetric data were used to evaluate the corrosion rate (CR), surface coverage (θ), and inhibition efficiency ($IE$%). For penetration-rate conversions, the density of the underlying low-carbon steel substrate (7.86g·$cm^{-3}$) was applied; the influence of the thin electrolytic tin coating (≈2 μm) relative to the overall specimen thickness is negligible.

$$\theta = \frac{W_0 - W_{inh}}{W_0} \tag{1}$$

$$IE\% = \frac{W_0 - W_{inh}}{W_0} \times 100 \tag{2}$$

where $W_o$ represents the weight loss in the absence of the inhibitor, and Winh is the weight loss in the presence of the inhibitor. The corrosion rate was determined from the measured weight loss and the corresponding decrease in thickness, expressed in mg·$cm^{-2}$·$h^{-1}$ , using Eq. (3):

$$CR = \frac{\Delta W}{A \times t} \tag{3}$$

### 2.5. Electrochemical measurements

#### 2.5.1. Open circuit potential (OCP)

The open circuit potential (OCP) was monitored using a high-impedance millivoltmeter to track changes in the working electrode potential over time under undisturbed conditions. This measurement provides insight into the electrochemical behavior of the metal/solution interface and helps assess spontaneous corrosion processes as well as the possible formation of protective surface films. The attainment of a stable OCP value indicates that the system has reached a quasi-steady state, corresponding to a balance between anodic and cathodic reactions. Changes in the OCP observed in the presence of corrosion inhibitors can be used to infer their inhibition mechanism, whether predominantly anodic, cathodic, or mixed.

#### 2.5.2. Potentiodynamic polarization test

The potentiodynamic polarization curves of tinplate were obtained in SBOB solution containing various concentrations of BPE, using a scan rate of 1 mV/s starting from the corrosion potential ($E_{corr}$). The corrosion current density ($I_{corr}$) values were determined through the Tafel extrapolation method. The inhibition efficiency (EI%) based on the corrosion current density was then calculated using the following Eq. (4):

$$EI\% = \left(\frac{I_0 - I_{inh}}{I_0}\right) \times 100 \tag{4}$$

$I_0$ and $I_{inh}$ correspond to the corrosion current densities measured in the absence and in the presence of BPE, respectively.

#### 2.5.3. Electrochemical impedance spectroscopy

The electrochemical measurements were carried out at room temperature using a Versa Stat 3 potentiostat connected to a standard three-electrode cell. A saturated calomel electrode was used as the reference electrode, and a platinum electrode served as the counter electrode. The working electrode was a tinplate sample with an exposed surface area of 1 $cm^2$. Before each experiment, the working electrode was cleaned by rinsing it with distilled water, followed by acetone, and then dried. It was then immersed in the SBOB solution containing various concentrations of BPE. Prior to recording any measurements, the electrode was allowed to stabilize at the open circuit potential ($E_{ocp}$) for 30 min. Electrochemical impedance spectroscopy (EIS) was carried out at the open-circuit potential ($E_{ocp}$), using a sinusoidal voltage signal of 10 mV (peak to peak). The frequency range was set from 100 kHz down to 10 mHz. The charge transfer resistance ($R_t$) and double-layer capacitance ($C_{dl}$) values were obtained from the Nyquist plots. The inhibition efficiency (IE%) was then calculated using the following Eq. (5):

$$IE\% = \left(\frac{R_{inh} - R_0}{R_{inh}}\right) \times 100 \tag{5}$$

$R_{inh}$ represents the charge transfer resistance in the presence of BPE, while $R_0$ corresponds to the charge transfer resistance measured in the uninhibited SBOB solution.

### 2.6. Total content of phenolic and flavonoid compounds

The purpose of this study was to evaluate both the total phenolic content (TPC) and the total flavonoid content (TFC) present in the n-BuOH fraction extracted from beetroot peels. The TPC was quantified using a modified version of the Ainsworth method [18]. The total flavonoid content (TFC) was measured following the Dowd procedure, using the modified protocol described by Arvouet-Grand et al. [19]. The

phenolic constituents of the n-BuOH fraction obtained from beetroot peel were analyzed using a Shimadzu 8040 UPLC-ESI-MS/MS system equipped with UFMS high sensitivity technology. The system configuration included a Nexera XR LC-20AD binary pump, a standard auto sampler, and a temperature-controlled compartment housing an Ultra-Force C18 column. Chromatographic separation was carried out under a gradient elution program, using two mobile phases: A (water with 0.1% formic acid) and B (methanol). The analyses were performed at a flow rate of 0.4 mL/min, with an injection volume of 5 µl. Phenolic compounds were identified in MRM mode, operating in both positive and negative ionization modes to achieve selective and sensitive detection. Calibration was performed using Sigma-Aldrich reference standards prepared in methanol at a concentration of 500 µg/L to ensure analytical accuracy. This method allowed for a comprehensive characterization of the phenolic profile of the n-BuOH fraction, providing valuable evidence of its potential corrosion-inhibiting properties, particularly in acidic environments.

### 2.7. Fourier transform infrared (FTIR)

Fourier transform infrared (FTIR) spectroscopy was employed to identify the main functional groups present in the studied extracts. The spectra were recorded over the wavenumber range of 4000–400 $cm^{-1}$ , and the characteristic absorption bands were examined to determine the functional groups involved in the corrosion inhibition process.

### 2.8. Optical microscopy and (SEM) analysis

The surface morphology of the metal samples was examined using optical microscopy and scanning electron microscopy (SEM). Observations were made on the bare metal surfaces before immersion to establish their initial condition, and again after immersion in solutions with and without the inhibitor. This allowed for a clear comparison of corrosion effects on the unprotected surfaces and the protective impact of the inhibitor.

### 2.9. Theoretical framework and computational methods

The selection of representative molecular models for the theoretical investigation was guided by the experimental LC-MS characterization of the Beta vulgaris L. extract (Section 3.1). Among the identified constituents, cinnamic acid (CIA), p-coumaric acid (COA), and esculin hydrate (EH) were found to be the predominant bioactive compounds. Accordingly, these molecules were selected for Density Functional Theory (DFT) and Molecular Dynamics (MD) simulations in order to evaluate their possible contribution to the experimentally observed corrosion inhibition performance. Considering the acidic conditions of the simulated black olive brine solution (pH = 4), protonated species were also taken into account. The protonation sites were selected according to proton affinity and basicity considerations reported in previous studies [11,12]. Consequently, both neutral and protonated forms (P-CIA and P-COA) were investigated to better represent the chemical environment of the corrosive medium. All quantum chemical calculations were carried out using the B3LYP functional in combination with the 6–31 G(d) basis set [20]. Solvent effects were considered through the conductor-like polarizable continuum model (CPCM), allowing the aqueous phase to be simulated under realistic corrosion conditions [21, 22]. Geometry optimizations and electronic structure calculations were performed using the Gaussian09 package [23].

Several global quantum chemical descriptors were determined, including ionization potential (IP), electron affinity (EA), electronegativity (χ), chemical hardness (η), softness (σ), electrophilicity index (ω), and the HOMO–LUMO energy gap (ΔE) [24]. These descriptors are commonly employed to evaluate molecular reactivity, charge-transfer capability, and adsorption tendency toward metallic surfaces [14,15]. The corresponding equations are expressed as follows [25–27]:

$$IP = - E_{HOMO} \quad (6)$$

$$EA = - E_{LUMO} \quad (7)$$

$$\Delta E = E_{LUMO} - E_{HOMO} \quad (8)$$

$$\chi = (IP + EA) / 2 = - (E_{HOMO} + E_{LUMO}) / 2 \quad (9)$$

$$\eta = (IP - EA) / 2 = (E_{LUMO} - E_{HOMO}) / 2 \quad (10)$$

$$\sigma = 1 / \eta \quad (11)$$

$$\omega = \chi^2 / 2\eta \quad (12)$$

To further examine the interaction between the inhibitor molecules and metallic surfaces, the fraction of transferred electrons (ΔN) was calculated according to:

$$\Delta N = (\varnothing_M - \chi_{inh})/[2 \quad (\eta_M + \eta_{inh})] \quad (13)$$

where $\Phi_{surface}$ represents the work function of the corresponding metallic surface, in order to account for the heterogeneous nature of the tinplate system, calculations were performed using literature work-function values associated with Fe(110), $S_n$(001), and $S_nO_2$(001) surfaces [28]. The work-function values used were $\Phi_M = 4.82$ eV for Fe(110), 4.75 eV for $SnO_2$(001) and 4.42 eV for Sn(001); the chemical hardness of the bulk metal ($\eta_M$) was taken as zero, the metallic surface being treated as a perfect electron reservoir. Following the usual convention, $\Delta N > 0$ corresponds to a net electron transfer from the inhibitor towards the metal, whereas $\Delta N < 0$ corresponds to a net transfer in the opposite direction. This parameter provides useful information regarding charge redistribution and electron-transfer tendencies at the inhibitor/metal interface [16,29].

### 2.10. Reactive site analysis: fukui indices and electrostatic potential (ESP)

To identify the reactive sites within the inhibitor molecules, Fukui indices were calculated. These indices identify regions that are more likely to undergo electrophilic, nucleophilic, or radical attacks, depending on changes in electron density resulting from electron addition or removal [30,31]. The Fukui indices are defined as follows. For a nucleophilic attack (addition of an electron) on atom k:

$$f_k^{+} = q_k\ (N + 1) - q_k\ (N) \quad (14)$$

For an electrophilic attack (removal of an electron) on atom k:

$$f_k^{-} = q_k\ (N) - q_k\ (N - 1) \quad (15)$$

For a radical attack (average variation) on atom k:

$$f_k^{0} = [q_k\ (N + 1) - q_k\ (N - 1)] / 2 \quad (16)$$

Where $q_k$(N), $q_k$(N + 1), and $q_k$(N-1) represent the atomic charges on atom k in the neutral, anionic, and cationic states, respectively, these indices allow for the identification of sites with the highest probability of interaction with the metal surface, thus determining the preferential localization of inhibition.

Furthermore, molecular electrostatic potential (ESP) maps were generated to visualize the distribution of electronic charge around the molecule, allowing for the identification of nucleophilic and electrophilic regions. By combining Fukui indices and ESP analysis, the study effectively identifies the active sites responsible for metal-surface interactions. It helps explain how inhibitors provide corrosion resistance through specific interactions at the molecular level [32].

### 2.11. Molecular dynamics (MD) simulations

Molecular dynamics (MD) simulations are an effective tool for

studying the behavior of inhibitor molecules on metal surfaces under varying thermodynamic conditions, such as temperature and pressure fluctuations. In this study, MD simulations were performed using the Forcite module in Materials 2023 in order to investigate the adsorption behavior of the inhibitor molecules on metallic surfaces [33]. The simulations were carried out in the presence of water molecules together with $Na^+$ and $Cl^-$ ions to reproduce the electrolyte environment of the corrosive medium. All simulations were conducted under the NVT ensemble at 300 K using the Andersen thermostat, with a total simulation time of 200 ps. Interatomic interactions were described using the COMPASS III force field. To account for the multi-surface nature of tinplate systems, adsorption simulations were performed on Fe(110), Sn (001), and $SnO_2$(001) surfaces using identical simulation parameters to ensure consistency and comparability of the obtained adsorption data. The dimensions of the simulation cells were adjusted according to the crystallographic characteristics of each surface.

## 3. Results and discussion

### 3.1. Characterization of BPE by UPLC–MS

The beetroot peel extract was analyzed using UPLC–ESI–MS/MS, which enabled the precise identification and characterization of its phenolic constituents. As shown in Table 2 and illustrated in Fig. 1, among the phenolic constituents identified and quantified under the LC–MS/MS conditions used, cinnamic acid showed the highest relative contribution (76.60%), followed by p-coumaric acid (11.39%) and esculin hydrate (9.00%).

These compounds constitute the predominant fraction of the extract. In addition to these major components (Fig. 1), several other phenolic molecules were detected in smaller proportions (less than 1%), including folic acid, Ferulic acid, quercetin, Rutine, Hespertin, Naringenin, and Oleanolic acid. Cinnamic acid and p-coumaric acid, both belonging to the hydroxycinnamic acid family, are characterized by their conjugated aromatic rings and the presence of hydroxyl and carboxyl functional groups. These structural features enhance their ability to neutralize free radicals and chelate reactive metal ions. As a result, they help reduce oxidation processes occurring on the metal surface [34].

In turn, esculin, a coumarin-derived glycoside, also exhibits notable antioxidant activity due to its phenolic functional groups. This compound contributes to the stabilization of the metal surface by promoting the formation of a protective organic film, thereby enhancing the overall corrosion-inhibiting effectiveness of the extract [35,36].

**Table 2**
Relative composition of the phenolic constituents identified in the analyzed BPE fraction by UPLC–MS/MS.

| N° | Constituents | *m/z* | Relative phenolic composition (%) |
|---|---|---|---|
| 1 | Acid coumaric | 165.1000 > 101.2000 | 11.39 |
| 2 | 4-mythoxybenzoic acid | 153.0500 > 70.7500 | 0.85 |
| 3 | Beta carotene | 537.2000 > 23.1000 | 0.17 |
| 4 | Esculin hydrate | 359.1000 > 295.1500 | 9.00 |
| 5 | Rutine | 611.2000 > 73.2000 | 0.13 |
| 6 | valinin | 153.1000 > 93.2000 | 0.043 |
| 7 | Cinnamic acid | 149.0500 > 84.7500 | 76.60 |
| 8 | Hespertin | 300.9000 > 255.2500 | 0.39 |
| 9 | Quercitine | 302.9000 > 270.9000 | 0.20 |
| 10 | Oleanolic acid | 457.2000 > 425.2000 | 0.25 |
| 11 | Naringénine | 272.9500 > 177.0000 | 0.05 |
| 12 | Folic acid | 442.9000 > 323.4500 | 0.680 |
| 13 | Caffein | 195.1000 > 137.9000 | 0.029 |
| 14 | Salysilic Acid | 137.1000 > 93.1500 | 0.017 |
| 15 | Thymol | 151.7500 > 88.1000 | 0.030 |
| 16 | Merycetin | 336.2500 > 46.1500 | 0.015 |
| 17 | Ferulic acid | 194.9000 > 177.1500 | 0.10 |

### 3.2. Characterization of BPE by FT-IR

The FTIR spectra of beet peel extract (BPE) recorded before and after contact with the tinplate surface are presented in Fig. 2. The spectrum of the pure extract exhibits a broad absorption band centered at approximately 3250 $cm^{-1}$, mainly attributed to O–H stretching vibrations associated with phenolic and hydrogen-bonded hydroxyl groups [37, 38]. A band around 2990 $cm^{-1}$ is assigned to aliphatic C–H stretching vibrations. In the region near 1600 $cm^{-1}$, a broad overlapping feature may include contributions from aromatic C═C vibrations and conjugated oxygen-containing functionalities [39,40]. However, the characteristic carbonyl stretching band expected for free aromatic carboxylic acids in the 1680–1710 $cm^{-1}$ region is not clearly resolved as a distinct intense peak. Because BPE is a complex multicomponent extract, band overlap, hydrogen bonding, and matrix effects may contribute to broadening or masking of individual absorptions. Therefore, the band near 1600 $cm^{-1}$ cannot be assigned unambiguously to a specific C═O vibration.

Additional bands observed around 1350 and 1000 $cm^{-1}$ are consistent with vibrations involving C–O–H and C–O functionalities [37–40]. After contact with the tinplate surface, slight changes in band position and intensity are observed, particularly in the O–H region and in bands associated with oxygen-containing groups. These changes are consistent with the involvement of polar functional groups in interfacial adsorption. However, the FTIR variations alone do not constitute direct evidence of specific coordination or chemical-bond formation and are therefore interpreted together with the electrochemical, SEM–EDX, and computational results.

### 3.3. Weight loss measurements

The corrosive behavior of tinplate in the presence of different concentrations of BPE extract was evaluated using the weight loss method, in order to examine the influence of inhibitor concentration on the corrosion rate and inhibition efficiency. The corresponding experimental results are summarized in Table 3, while Fig. 3 illustrates the variation of the corrosion rate (CR) and the inhibition efficiency (IE%) as a function of the inhibitor concentration. The results show a marked decrease in the corrosion rate as the extract concentration increases, indicating a progressive adsorption of the bioactive molecules onto the metal surface. This adsorption promotes the formation of a protective film that effectively limits the contact between the tinplate and the corrosive medium, thereby enhancing its resistance to degradation. The inhibition efficiency increases progressively with the concentration of the extract, reaching a maximum value of 94.8% at 300 mg/L, which corresponds to the optimal concentration at which the tinplate surface is nearly saturated with inhibitor molecules.

Beyond this concentration, a slight decrease in efficiency is observed, likely due to surface saturation or partial desorption of the adsorbed species, which weakens the protective film formed on the metal surface. As a result, a small reduction in IE% is noted at higher inhibitor concentrations. This trend is consistent with previous studies, which have also reported that excessively high inhibitor concentrations may lead to a decline in overall inhibition performance [41].

### 3.4. Electrochemical analysis

#### 3.4.1. Open circuit potential (OCP)

Fig. 4 illustrates the variation of the Open Circuit Potential (OCP) recorded for tinplate in both the uninhibited solution and in the presence of different concentrations of BPE. In the absence of the inhibitor, the OCP stabilizes near –485 mV/SCE, reflecting an active dissolution of the metal and the dominance of anodic corrosion processes. Upon introducing the beetroot peel extract, the potential shifts toward more positive values, reaching around –435 mV/SCE at a concentration of 100 mg/l. This positive shift indicates the adsorption of phytochemical

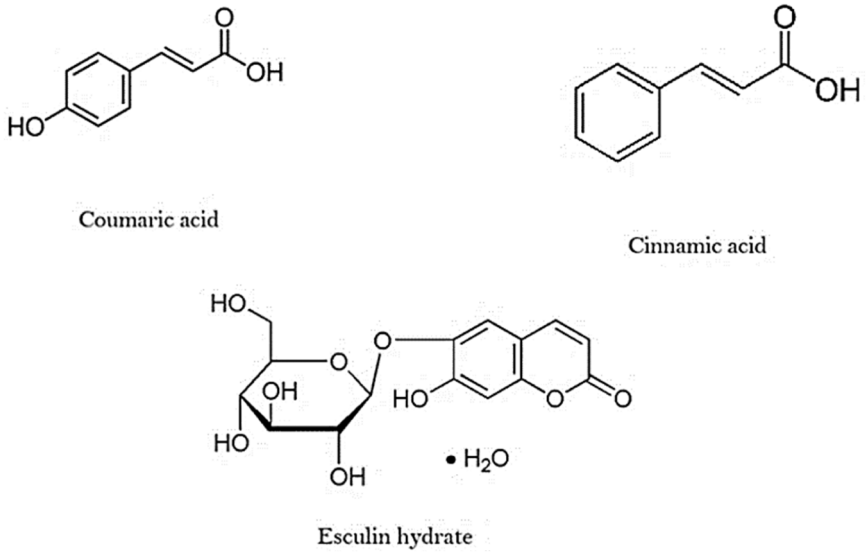


**Fig. 1.** Chemical structures of the main bioactive compounds identified in the BPE through LC–MS/MS analysis.

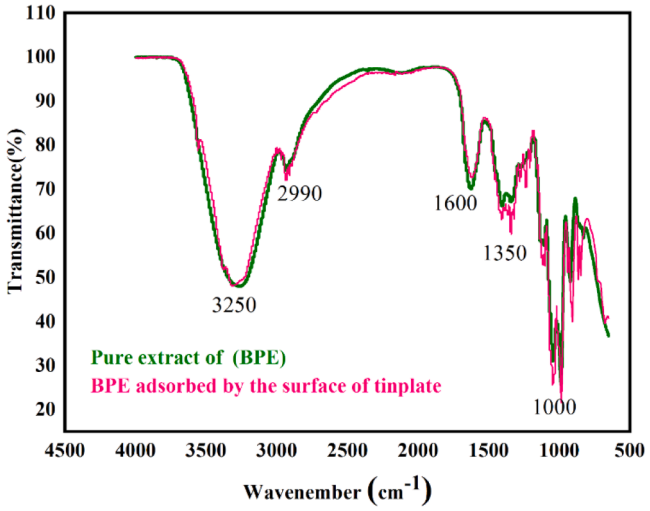


**Fig. 2.** FTIR spectra of BPE before and after contact with the tinplate surface.

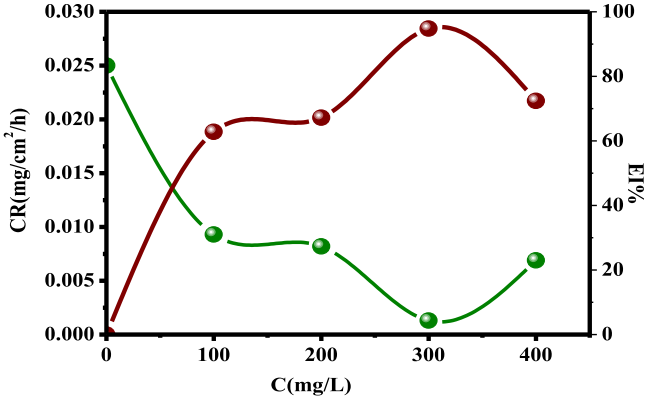


**Fig. 3.** Variation of weight loss with BPE concentration after 72 h of tinplate immersion in the SBOB solution.

**Table 3**
Average corrosion parameters and inhibition efficiencies (IE%) of BPE on tinplate in the SBOB solution, determined from weight loss measurements.

| C (mg/L) | CR (mg/cm$^2$/h) | θ | EI (%) |
|---|---|---|---|
| 0 | 0.0250 ± 0.0012 | - | - |
| 100 | 0.0093 ± 0.0005 | 0.628 | 62.8 |
| 200 | 0.0082 ± 0.0004 | 0.672 | 67.2 |
| 300 | 0.0013 ± 0.0001 | 0.948 | 94.8 |
| 400 | 0.0069 ± 0.0004 | 0.724 | 72.4 |

constituents from the extract onto the tinplate surface, leading to the formation of a protective layer that slows down the corrosion reactions. As the inhibitor concentration increases (from 200 to 400 mg/L), the OCP becomes more stable, reflecting an enhanced passivation of the metal surface and a reduction in the corrosion rate.

The most stable potential is observed at 300 mg/L, indicating the formation of a compact and uniform protective film, resulting from the effective adsorption of the active organic molecules onto the tinplate surface. After extended immersion, a slight shift of the potential toward more negative values is noted, which can be attributed to the gradual

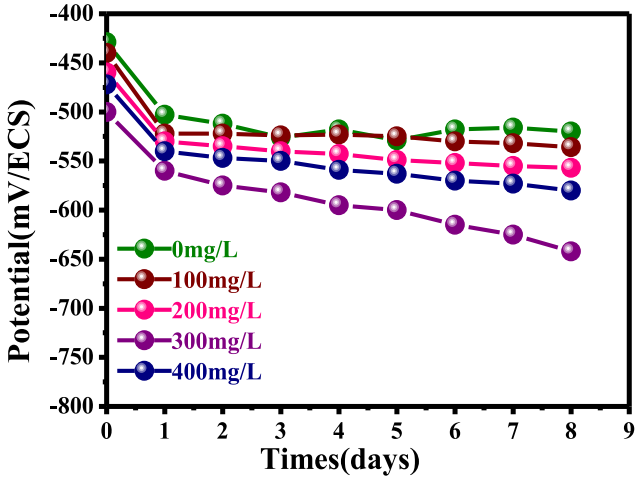


**Fig. 4.** Variation of the open circuit potential (OCP) over time for tinplate in the SBOB solution, in the presence of different concentrations of BPE, during an immersion period of 8 days.

weakening of the adsorbed film under the influence of the corrosive environment. Moreover, the OCP displacement remains relatively

limited over the investigated concentration range. However, OCP shifts alone are insufficient to classify the inhibitor mechanism [42]. The anodic, cathodic, or mixed character of BPE is therefore assessed primarily from the potentiodynamic polarization behavior discussed in Section 3.4.2.

### 3.4.2. Potentiodynamic polarization technique (PDP)

The electrochemical analysis of tinplate in the presence of different concentrations of BPE was carried out using the potentiodynamic polarization technique. This method allows the evaluation of the extract's influence on both the anodic and cathodic reactions occurring at the metal surface. The main electrochemical parameters derived from the polarization curves are summarized in Table 4, while Fig. 5 illustrates the evolution of the polarization curves for the various inhibitor concentrations.

Based on Fig. 5 and Table 4, a clear change in the electrochemical behavior of tinplate is observed in the presence of different concentrations of beetroot peel extract. The corrosion current density ($i_{corr}$) progressively decreases as the inhibitor concentration increases, dropping from 1.412 μA/cm$^2$ in the absence of the extract to 0.078 μA/cm$^2$ at a concentration of 300 mg/L. This decrease indicates a significant reduction in the corrosion rate ($V_{corr}$) and an optimal inhibition efficiency of 94.47%, confirming the effectiveness of the extract as a protective agent for tinplate.

The polarization parameters reveal a non-monotonic variation of the corrosion potential ($E_{corr}$) with BPE concentration. ($E_{corr}$) shifts from −639 mV for the uninhibited system to −477 and −439 mV at 100 and 200 mg L$^{-1}$ , respectively, before shifting to a more negative value of −600 mV at 300 mg L$^{-1}$ and −490 mV at 400 mg L$^{-1}$ . Therefore, the direction and magnitude of the ($E_{corr}$) shift should not be considered direct indicators of inhibition efficiency. More importantly, the marked decrease in corrosion current density ($i_{corr}$), together with the modification of both the anodic and cathodic branches of the polarization curves, indicates that BPE influences both partial corrosion reactions. This behavior supports its classification as a mixed-type inhibitor rather than as a predominantly anodic or cathodic inhibitor [43,44].

The polarization resistance ($R_p$) increases substantially in the presence of BPE and reaches its maximum value of 17,579 Ω·cm$^2$ at 300 mg L$^{-1}$ , concomitantly with the minimum ($i_{corr}$) value and the highest PDP inhibition efficiency (94.47%). These results are consistent with the formation of an adsorbed protective layer that reduces the electrochemically active area and limits the access of aggressive species to the tinplate/electrolyte interface [45]. At 400 mg L$^{-1}$ , the inhibition efficiency decreases to 71.42%, accompanied by a reduction in ($R_p$) and an increase in ($i_{corr}$). This decrease suggests that concentrations above the optimum do not provide additional protection and may alter the organization or stability of the adsorbed inhibitor layer; however, the polarization data alone do not allow a unique mechanism, such as desorption or steric effects, to be established [46]. Overall, the PDP results identify 300 mg L$^{-1}$ as the optimum BPE concentration under the investigated conditions and demonstrate that BPE suppresses both the anodic and cathodic corrosion processes of tinplate in SBOB.

**Table 4**
Kinetic corrosion parameters of tinplate obtained from the potentiodynamic polarization curves, in the absence and presence of the inhibitor.

| C (mg/L) | $E_{corr}$ (mV) | $i_{corr}$ (μA/cm$^2$) | $V_{corr}$ (μm/y) | θ | Rp (Ω.cm$^2$) | IE% |
|---|---|---|---|---|---|---|
| 0 | -639 ± 8,43 | 1.412 ± 0,06 | 162.73 | - | 713 ± 43 | - |
| 100 | -477 ± 10,76 | 0.542 ± 0,03 | 62.46 | 0.6162 | 6733 ± 53 | 61,62 |
| 200 | -439 ± 12,33 | 0.503 ± 0,05 | 57.97 | 0.6437 | 5628 ± 32 | 64,37 |
| 300 | -600 ± 11,56 | 0.078 ± 0,02 | 8.99 | 0.9447 | 17579 ± 123 | 94,47 |
| 400 | -490 ± 9,70 | 0.403 ± 0,07 | 46.50 | 0.7142 | 3581 ± 76 | 71,42 |

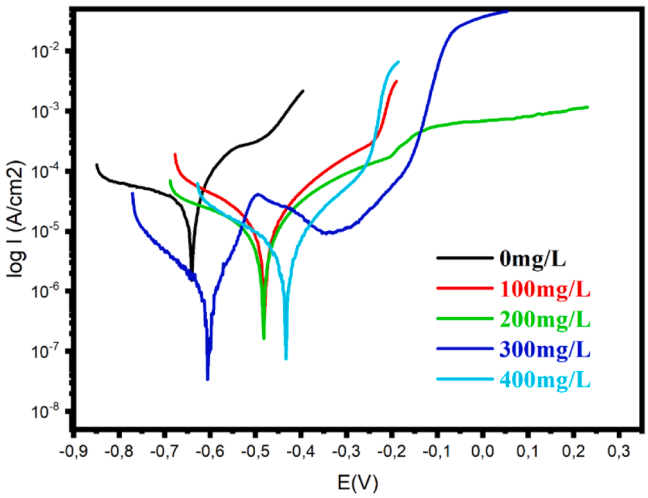


**Fig. 5.** Potentiodynamic polarization curves of tinplate samples immersed in the SBOB solution, showing the effect of different BPE concentrations in comparison with the uninhibited solution.

### 3.4.3. Electrochemical impedance spectroscopy (EIS)

Electrochemical impedance spectroscopy (EIS) measurements were conducted to evaluate the interfacial behavior and kinetics of the electrochemical processes occurring at the tinplate/electrolyte interface in both the absence and presence of various concentrations of BPE [47,48]. The impedance responses were recorded at the open-circuit potential ($E_{ocp}$) following a 30-min stabilization period. The corresponding Nyquist and Bode plots are displayed in Fig. 6. The Nyquist diagrams (Fig. 6a) exhibit depressed capacitive semicircles across the tested frequency range, indicative of a corrosion mechanism primarily controlled by interfacial charge-transfer processes. The departure from ideal semi-circular behavior (depressed loop with center positioned below the real axis) is characteristic of solid electrode surfaces and is generally attributed to microscopic roughness, chemical heterogeneity, and non-uniform current distribution [49].

As the concentration of BPE increases up to 300mg·L$^{-1}$, the diameter of the capacitive arc expands markedly, indicating a substantial enhancement of the charge-transfer resistance ($R_{ct}$) and a corresponding suppression of metal dissolution. At 300mg·L$^{-1}$, the inhibition efficiency reaches its maximum value (99.38%), evidencing the formation of a dense, protective organic barrier on the tinplate surface [50]. At a higher concentration (400mg·L$^{-1}$), a slight decrease in the semicircle diameter is observed, reflecting partial desorption, steric hindrance, or structural rearrangement of the adsorbed species once surface saturation is exceeded. The Bode representations (Figs. 6b and 6c) corroborate these observations. In the low-frequency limit, the absolute impedance modulus ($|Z|$) increases by more than two orders of magnitude in the presence of the inhibitor, reaching its peak value at 300mg·L$^{-1}$, in full agreement with the trend in polarization resistance. In the Bode phase-angle plots, the phase angle broadens and shifts toward higher values over an extended intermediate frequency range with increasing BPE concentration, demonstrating enhanced capacitive behavior and film compactness at the electrode/electrolyte interface [51,52]. The presence of a single broad time-constant signature across the spectrum indicates that the interfacial response is governed by charge transfer coupled with dielectric barrier formation across the protective adsorbate layer. To quantitatively evaluate the impedance data, the experimental spectra were fitted using the equivalent electrical circuit (EEC) depicted in Fig. 7.

This circuit, with the structure $R_s(Q_{ad}[R_{ad}(Q_{ct}R_{ct})])$, consists of:

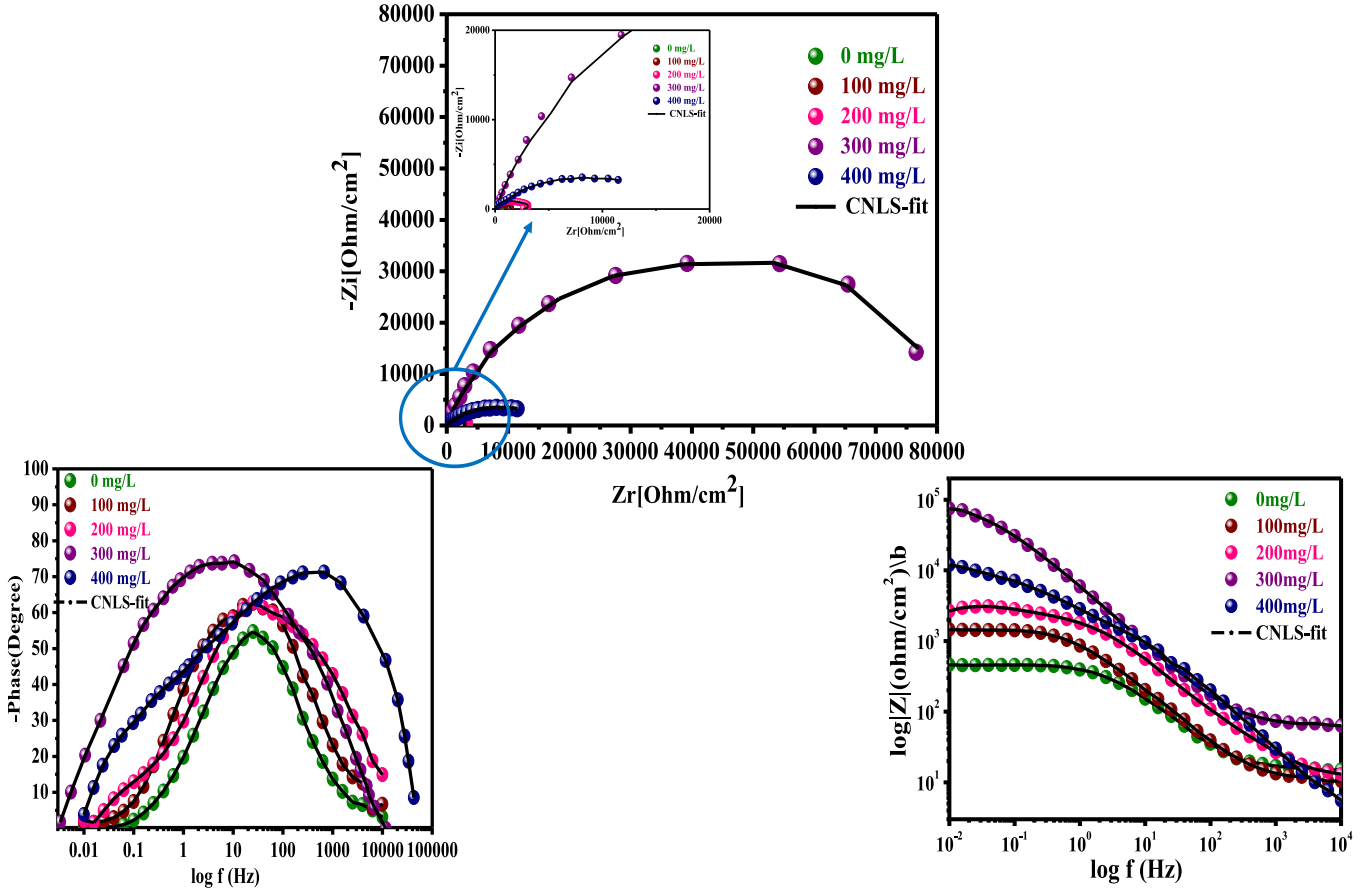


**Fig. 6.** Nyquist and Bode plots illustrating the electrochemical behavior of tinplate in the SBOB solution with the addition of BPE at different concentrations.

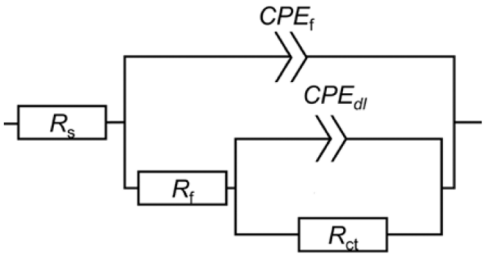


**Fig. 7.** Equivalent electrical circuit model used to interpret the EIS responses of tinplate in the SBOB solution, both in the absence and presence of the BPE inhibitor.

- the uncompensated solution resistance ($R_s$or$R_e$),
- the resistance of the outer adsorbed organic film ($R_{ad}$, tabulated as $R_f$ in the schematic), in parallel with a constant phase element ($Q_{ad}$ or $CPE_f$) representing the dielectric properties and non-ideal capacitance of the adsorbed layer,
- the inner charge-transfer resistance ($R_{ct}$) at the metal/film interface, in parallel with a second constant phase element ($Q_{ct}$ or $CPE_{dl}$) describing the electrochemical double layer.

Constant phase elements (CPE) were employed in place of pure capacitors to account for frequency dispersion arising from atomic-scale roughness, structural heterogeneity, and localized potential gradients. The impedance of a CPE is defined as $Z_{CPE} = [Q(j\omega)^n]^{-1}$, where Q is the CPE magnitude ($\Omega^{-1}\cdot s^n\cdot cm^{-2}$), $\omega$ is the angular frequency ($rad\cdot s^{-1}$), $j^2 = -1$, and $n$ is an empirical phase factor ($0 \leq n \leq 1$) reflecting interfacial non-ideality.

The fitted parameters obtained from the EEC are summarized in Table 5.

The charge-transfer resistance ($R_{ct}$) rises dramatically from 449Ω·cm$^2$ for the uninhibited medium to 73,164Ω·cm$^2$ at 300 mg·L$^{-1}$ of BPE. Concurrently, the apparent CPE coefficients ($Q_{ad}$ and $Q_{ct}$) exhibit a pronounced decrease, which can be qualitatively interpreted in terms of the progressive replacement of high-dielectric water molecules and aggressive chloride ions by adsorbed organic constituents possessing lower dielectric constants, alongside an effective increase in the electrical double-layer thickness [53]. A comparison between the charge-transfer resistance derived from EIS ($R_{ct} = 73,164\Omega\cdot cm^2$ at 300mg·L$^{-1}$) and the polarization resistance obtained from potentiodynamic polarization ($R_p = 17,579\Omega\cdot cm^2$) reveals a notable difference. Such disparity is commonly encountered in electrochemical corrosion studies and stems directly from the distinct perturbation regimes of the two methods: EIS probes the unperturbed interface under steady-state conditions at the open-circuit potential using small-amplitude AC signals (10mV), thereby preserving the integrity of the adsorbed organic layer. Conversely, potentiodynamic sweeps impose significant DC potential polarizations away from equilibrium, which can induce partial desorption, field-assisted perturbation of the adsorbate layer, or altered interfacial kinetics during Tafel extrapolation. Furthermore, the pronounced increase in $R_{ct}$ at 300 mg·L$^{-1}$ aligns with an optimal surface coverage where active dissolution sites are effectively blocked by the adsorbed phytochemical constituents. The subsequent reduction in $R_{ct}$ at 400 mg·L$^{-1}$ is consistent with the trend observed in polarization and weight-loss measurements, likely arising from steric repulsion, molecular rearrangement, or partial desorption phenomena occurring once optimal surface saturation is exceeded. Fig. 8 displays the evolution of

**Table 5**
Nyquist and Bode impedance diagrams obtained for tinplate immersed in the SBOB medium, comparing the behavior of the system in the presence of various concentrations of BPE.

| $C_{inh}$ (mg/l) | $R_e$ ($\Omega \cdot cm^{-2}$) | $n_1$ | $Q_{ct}$ $\Omega^{-1}cm^{-2n}$ $S^n.10^{-5}$ | $R_{ct}$ ($\Omega \bullet cm^{-2}$) | $n_2$ | $Q_{ad}$ $\Omega^{-1}cm^{-2n}$ $S^n.10^{-5}$ | $R_{ad}$ ($\Omega \bullet cm^{-2}$) | IE (%) | Error (%) | $X^2.10^{-4}$ |
|---|---|---|---|---|---|---|---|---|---|---|
| 0 | 15.15 ± 0,05 | 0.74 | 207 ± 0.23 | 449 ± 21 | 0,72 | 21.55 ± 0.08 | 500 ± 28.7 | - | 4.56 | 5 |
| 100 | 10.59 ± 0,09 | 0.80 | 10.66 ± 0.08 | 1255 ± 42 | 0,80 | 8.18 ± 0.05 | 1400 ± 53 | 64.28 | 3.20 | 2 |
| 200 | 11.25 ± 1,04 | 0.81 | 8.17 ± 0.05 | 2804 ± 49 | 0.84 | 4.65 ± 0.02 | 3002 ± 48 | 83.34 | 4.55 | 3 |
| 300 | 65.12 ± 0,07 | 0.85 | 3.69 ± 0.02 | 73164 ± 107 | 0.72 | 1.29 ± 0.03 | 73300 ± 104,23 | 99.38 | 4.32 | 4 |
| 400 | 29.7 ± 0,06 | 0.83 | 7.95 ± 0.03 | 15218 ± 85 | 0.78 | 2.09 ± 0.07 | 15247 ± 76 | 96.72 | 5.22 | 6 |

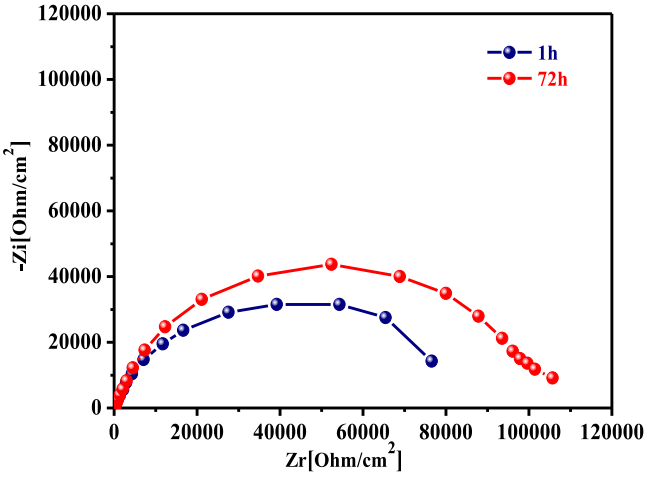


**Fig. 8.** Nyquist plots showing how immersion time affects the corrosion behavior of tinplate in the SBOB solution containing 300 mg/L of BPE.

Nyquist diagrams recorded for tinplate in the SBOB solution containing 300 $mg \cdot L^{-1}$ of BPE over immersion periods up to 72 h.

The capacitive arc radius increases monotonically with exposure time, showing that the protective layer does not degrade upon prolonged immersion, but rather consolidates. During the initial stages of immersion, the adsorbed organic film remains partially discontinuous, allowing limited ionic ingress. Over time, slow competitive adsorption and molecular reorganization of polyphenolic and aromatic constituents facilitate a more compact, cohesive organic film across active sites, confirming the long-term durability and barrier efficiency of the BPE layer on the tinplate surface in the simulated food brine medium [54, 55].

### 3.5. Adsorption behavior modeling

The investigation of adsorption isotherms provides critical mechanistic insight into the nature, strength, and energetics of the interactions established between the organic corrosion inhibitor molecules and the tinplate substrate. The degree of surface coverage (θ) at various BPE concentrations was calculated from the weight loss measurements using Eq. (1) and evaluated against several classical adsorption isotherm models, namely Langmuir, Temkin, Freundlich, and Frumkin (Fig. 9).

As illustrated in Fig. 9a and summarized in Table 6, the experimental data show an outstanding correlation with the Langmuir adsorption model, yielding a linear correlation coefficient ($R^2$) of 0.996. In comparison, the alternative isotherm models (Temkin, Freundlich, and Frumkin; Fig. 9b–d) exhibit significantly lower regression coefficients ($R^2 = 0.577 - -0.675$), confirming that the adsorption of BPE active compounds across the tinplate surface conforms predominantly to Langmuirian behavior.

The linear regression of $C_{inh}/\Theta$ versus $C_{inh}$ yields a slope of 1.15 and an adsorption equilibrium constant ($K_{ads}$) of 60.79 $L \cdot g^{-1}$. A slope close to unity is consistent with predominantly monolayer adsorption across energetically quasi-equivalent active sites. Nevertheless, the slight positive deviation from ideal unity (1.15) reflects the multi-component nature of the plant extract; it accounts for mutual lateral interactions (steric and dipole–dipole forces) among neighboring adsorbed molecules, as well as competitive adsorption among the predominant constituents (cinnamic acid, *p*-coumaric acid, and esculin hydrate) possessing different molecular volumes and adsorption affinities. The high magnitude of $K_{ads}$ (60.79 $L \cdot g^{-1}$) underscores the strong adsorption affinity of the extract's bioactive constituents toward the tinplate substrate, ensuring the establishment of a coherent and stable protective barrier that restricts the diffusion of aggressive $Cl^-$ and $H^+$ ions toward the underlying metal.

The standard free energy of adsorption ($\Delta G^{\circ}_{ads}$) is related to the equilibrium adsorption constant via the thermodynamic relation:

$$\Delta G^{\circ}_{ads} = -RT\ln(C_{solvent} \cdot K_{ads}) \quad (17)$$

where $R$ is the universal gas constant (8.314 $J \cdot mol^{-1} \cdot K^{-1}$), $T$ is the absolute temperature (298.15 K), and $C_{solvent}$ is the molar concentration of water in the bulk solution (55.5 $mol \cdot L^{-1}$, corresponding to ≈ 1000 $g \cdot L^{-1}$).

Because BPE is a multi-component plant extract, $K_{ads}$ was experimentally determined in mass units ($L \cdot g^{-1}$). To ensure rigorous thermodynamic dimensional consistency when applying the standard reference state of 55.5 $mol \cdot L^{-1}$, $K_{ads}$ was converted to molar units ($L \cdot mol^{-1}$) using the weighted average molar mass of the identified bioactive phenolic constituents ($M_{eff} \approx 150.3$ $g \cdot mol^{-1}$, taking into account cinnamic acid, *p*-coumaric acid, and esculin hydrate according to their relative LC-MS proportions (Table 2):

$$K_{ads,molar} = K_{ads} \times M_{eff} = 60.79\ L \cdot g^{-1} \times 150.3\ g \cdot mol^{-1} \approx 9137\ L \cdot mol^{-1} \quad (18)$$

Substituting $K_{ads,molar}$ into the standard thermodynamic equation gives:

$$\Delta G^{\circ}_{ads} = -8.314 \times 298.15 \times \ln(55.5 \times 9137) \times 10^{-3} \approx -32.5 kJ \cdot mol^{-1} \quad (19)$$

Alternatively, if evaluated directly using the standard mass-concentration reference frame of water (1000 $g \cdot L^{-1}$):

$$\Delta G^{\circ}_{ads} = -RT\ln(1000 \cdot K_{ads}) = -8.314 \times 298.15 \times \ln(1000 \times 60.79) \times 10^{-3} = -27.29 kJ \cdot mol^{-1}$$

The negative sign of $\Delta G^{\circ}_{ads}$ demonstrates the thermodynamic spontaneity of the adsorption process and the stability of the adsorbed film on the tinplate surface. Generally, values of $\Delta G^{\circ}_{ads}$ up to $-20$ $kJ \cdot mol^{-1}$ are associated with physical adsorption (physisorption) governed by electrostatic interactions between charged species and the charged metal surface, whereas values more negative than $-40$ $kJ \cdot mol^{-1}$ indicate chemisorption involving charge sharing or coordinate covalent bonding between inhibitor heteroatoms and vacant metal d-orbitals. The obtained value of $\Delta G^{\circ}_{ads}$ (ranging between $-27.29$ and $-32.5$ $kJ \cdot mol^{-1}$ depending on the standard state convention adopted) lies unambiguously within the intermediate range.

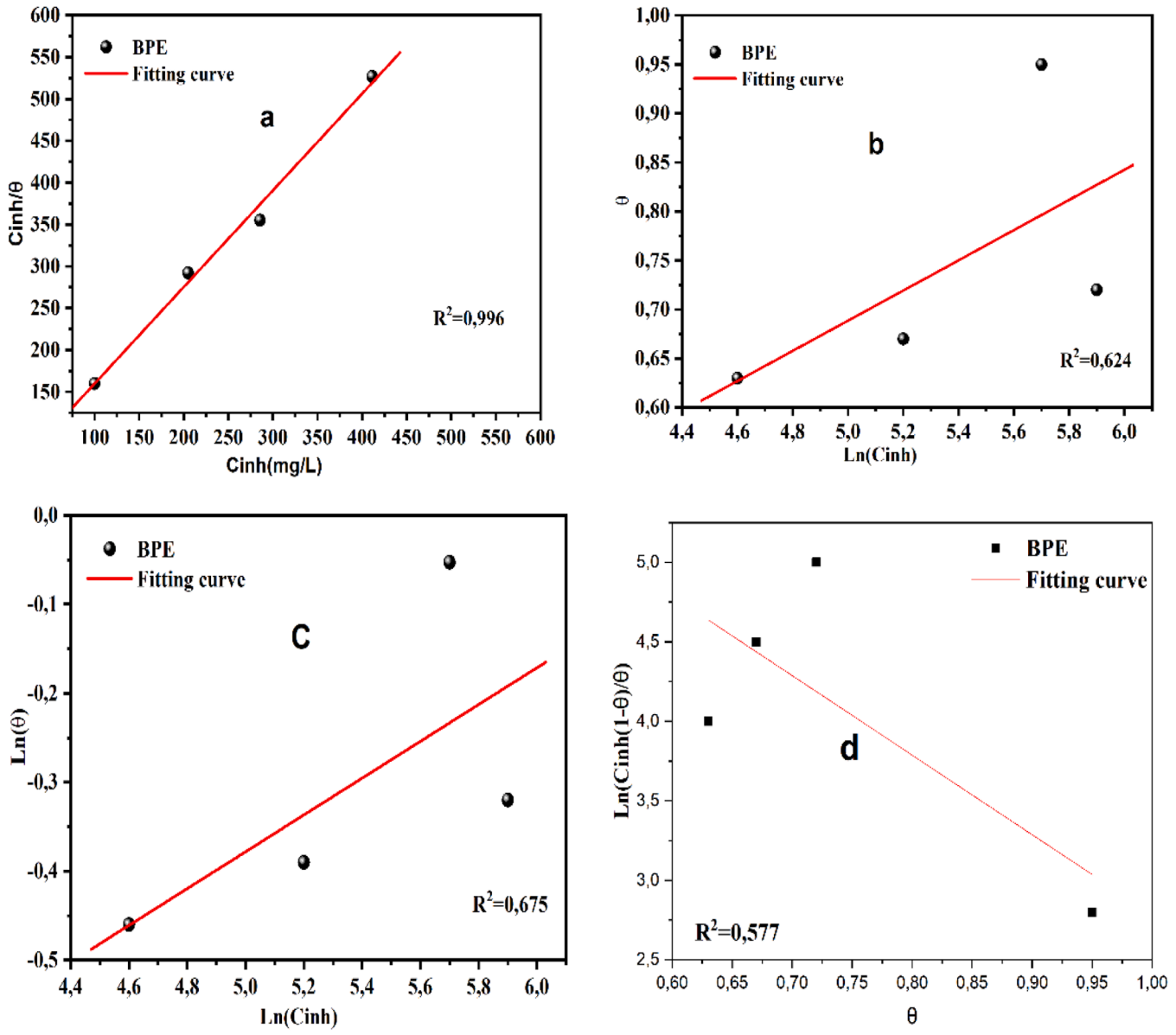


**Fig. 9.** Adsorption isotherms of BPE on the tinplate surface in SBOB solution: (a) Langmuir model, (b) Temkin model, (c) Freundlich model, and (d) Frumkin model.

**Table 6**
Values of parameters describing the adsorption behavior of the inhibitor on the tinplate surface.

| | $K_{ads}$(L/g) | Slope | $R^2$ | $\Delta G^{\circ}_{ads}$(KJ/mol) |
|---|---|---|---|---|
| BPE (300 mg/L) | 60.79 | 1.15 | 0.996 | -27.290 |

This demonstrates that the adsorption of BPE constituents onto the tinplate surface proceeds via a comprehensive **mixed-type mechanism** combining both physisorption and chemisorption. Electrostatic anchoring of protonated and polar moieties operates concurrently with chemical coordination, in which unshared electron pairs on oxygen-containing functionalities and delocalized π-electrons from aromatic rings interact directly with vacant metallic orbitals. This mixed-adsorption mechanism is corroboratively supported by the peak shifts observed in FTIR spectra (Section 3.2), the interfacial retention of iron under corrosive conditions revealed by SEM-EDX (Section 3.6), and the donor–acceptor electronic properties revealed by DFT Fukui descriptors and multi-surface MD simulations (Sections 3.7–3.10).

### *3.6. Scanning electron microscopy (SEM) analysis*

The microscopic (Fig. 10) observations, along with the EDX elemental analyses (Fig. 11), and the data in Table 7, help assess the protective effect of the beetroot peel extract (BPE) on the tinplate surface exposed to the SBOB solution. Without the inhibitor, the metal surface shows significant deterioration, with clear signs of localized corrosion, pitting, and increased roughness, indicating intense corrosive attack. This observation is supported by the EDX results, which reveal elevated levels of oxygen (7.33%) and chlorine (1.32%), confirming the presence of corrosion products such as iron oxides and iron chlorides. In contrast, when 300 mg/L of BPE extract is added, the tinplate surface appears noticeably smoother and more uniform, with no visible cracks or deposits. This suggests the formation of a stable and compact organic protective film. This film is formed through the adsorption of active compounds present in the BPE, particularly polyphenols, flavonoids, and nitrogen-containing molecules, which act as a combined physical and chemical barrier, effectively reducing the access of corrosive species to the metal surface.

The EDX analysis supports this observation, revealing a marked

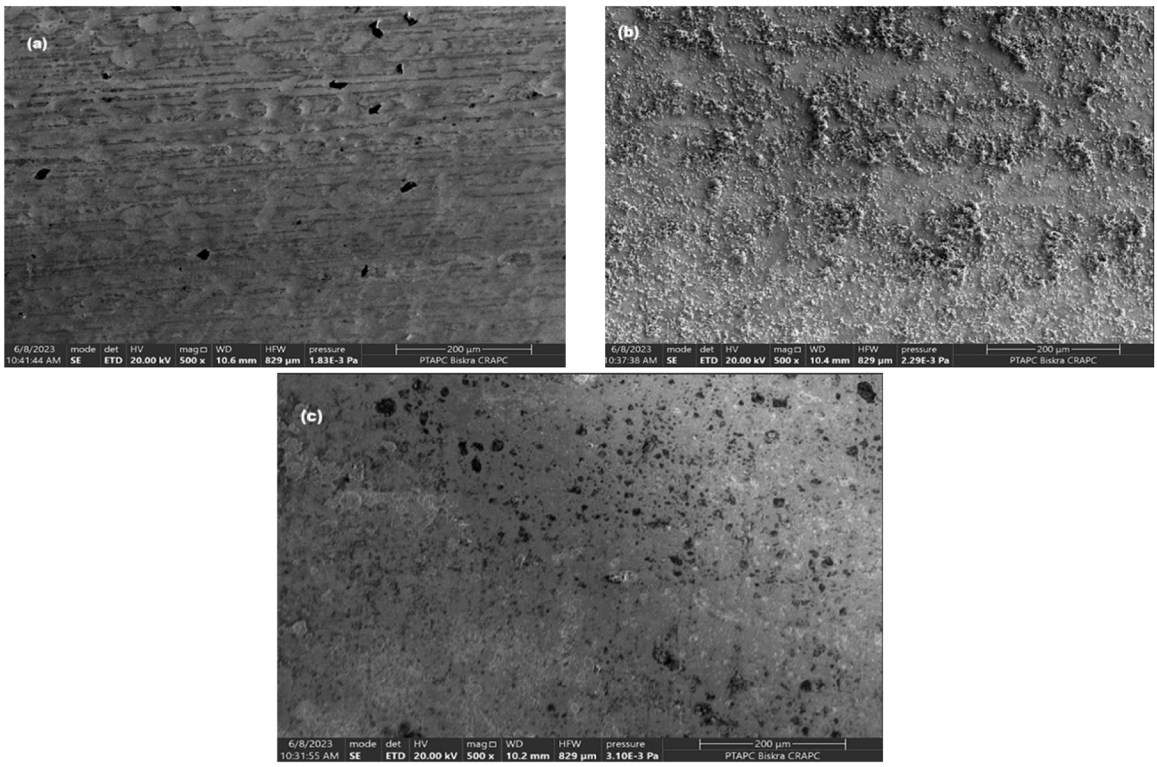


**Fig. 10.** SEM images of tinplate samples: (a) before exposure to the SBOB solution, (b) after 7 days of immersion in the SBOB solution without inhibitor, (c) after 7 days of immersion in the SBOB solution with the addition of 300 mg/L of inhibitor.

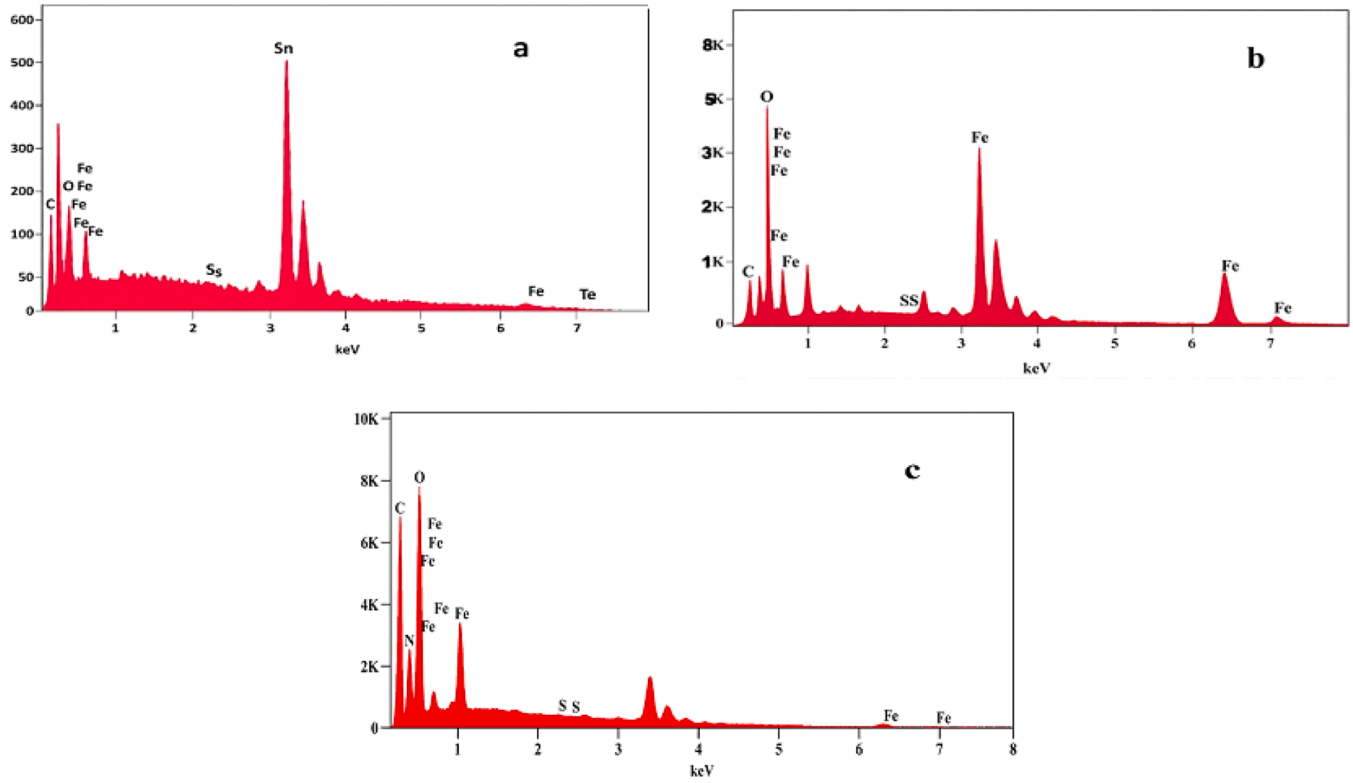


**Fig. 11.** EDX spectra of tinplate samples: (a) before immersion in the SBOB solution, (b) after 7 days of immersion in the SBOB solution, (c) after 7 days of immersion in the SBOB solution with 300 mg/L of inhibitor added.

decrease in corrosive elements (O, Na, Cl) and a significant increase in the iron content (from 20.25% to 50.34%).

This indicates that the metal surface is better preserved and less masked by corrosion products. The reversal between the bulk XRF

**Table 7**
Changes in the mass percentages of the main elements.

| specimen | C | O | Na | Cl | Sn | Fe |
|---|---|---|---|---|---|---|
| Metal | 10.32 | 4.78 | - | - | 44.78 | 1.48 |
| In the solution SBOB | 8.63 | 7.33 | 4.65 | 1.32 | 40 | 20.25 |
| In the solution SBOB with BPE | 6.54 | 4.85 | - | - | 35.43 | 50.34 |

composition (Table 1: Fe = 98.55%, Sn = 1.04%) and the unexposed-surface EDX composition (Table 7: Sn = 44.78%, Fe = 1.48%) is expected rather than contradictory: EDX probes only the outermost ~1–2 μm, comparable to or smaller than the ~2 μm electrolytic tin coating (Section 2.1), and therefore predominantly detects the tin overlayer, whereas XRF penetrates through to the steel core.

These findings clearly demonstrate that beetroot extract is highly effective as a green corrosion inhibitor, significantly limiting the oxidation of tinplate in the SBOB environment. Its inhibitory activity is mainly due to the adsorption of the extract's organic molecules onto the metal surface. This adsorption occurs through a mixed mechanism, involving both physical (electrostatic) interactions and chemical coordination between the functional groups of the molecules and iron atoms. As a result, a stable protective film is formed, which slows down both the anodic dissolution of the metal and the cathodic reduction reactions [56].

### 3.7. DFT analyses

#### 3.7.1. Frontier Molecular Orbital (FMO) Analysis

The electronic structure and reactivity of the organic corrosion inhibitors were examined in both their neutral and protonated forms using DFT at the B3LYP/6–31 G(d) level of theory. The optimized geometries and frontier molecular orbitals (HOMO and LUMO) for each species are presented in Fig. 12.

In the neutral state, the electron density of the HOMO is predominantly localized on the oxygen atoms and specific aromatic regions, indicating their role as potential electron-donating sites in interactions with the metal surface. Conversely, the LUMO is primarily distributed over the aromatic rings, which are identified as the most likely regions for electrophilic attack. This distribution of electronic density illustrates how the inhibitor's electronic structure affects its reactivity and charge transfer with the metal surface. Protonation shifts the HOMO and LUMO energy levels, altering the inhibitor's electron-donating and accepting properties.

Table 8 presents global quantum chemical descriptors of organic corrosion inhibitors, providing insight into their electronic properties and reactivity. The quantum chemical descriptors listed in Table 8 provide important insight into the electronic reactivity and charge-transfer capability of the investigated inhibitors. The relatively high EHOMO values indicate favorable electron-donating ability toward metallic surfaces, while the low ELUMO energies support electron-accepting interactions. Among the studied molecules, P-COA exhibits the smallest HOMO–LUMO energy gap (ΔE = 2.694 eV), together with the lowest hardness (η = 1.347 eV) and highest softness (σ = 0.742 eV), suggesting enhanced electronic reactivity and polarization capability. The electrophilicity index (ω) further indicates that the protonated species possess stronger charge-transfer tendencies compared with the neutral forms.

Overall, the DFT results suggest that protonation modifies the electronic structure of the inhibitors and may enhance their reactivity toward metallic surfaces under acidic conditions. However, the actual

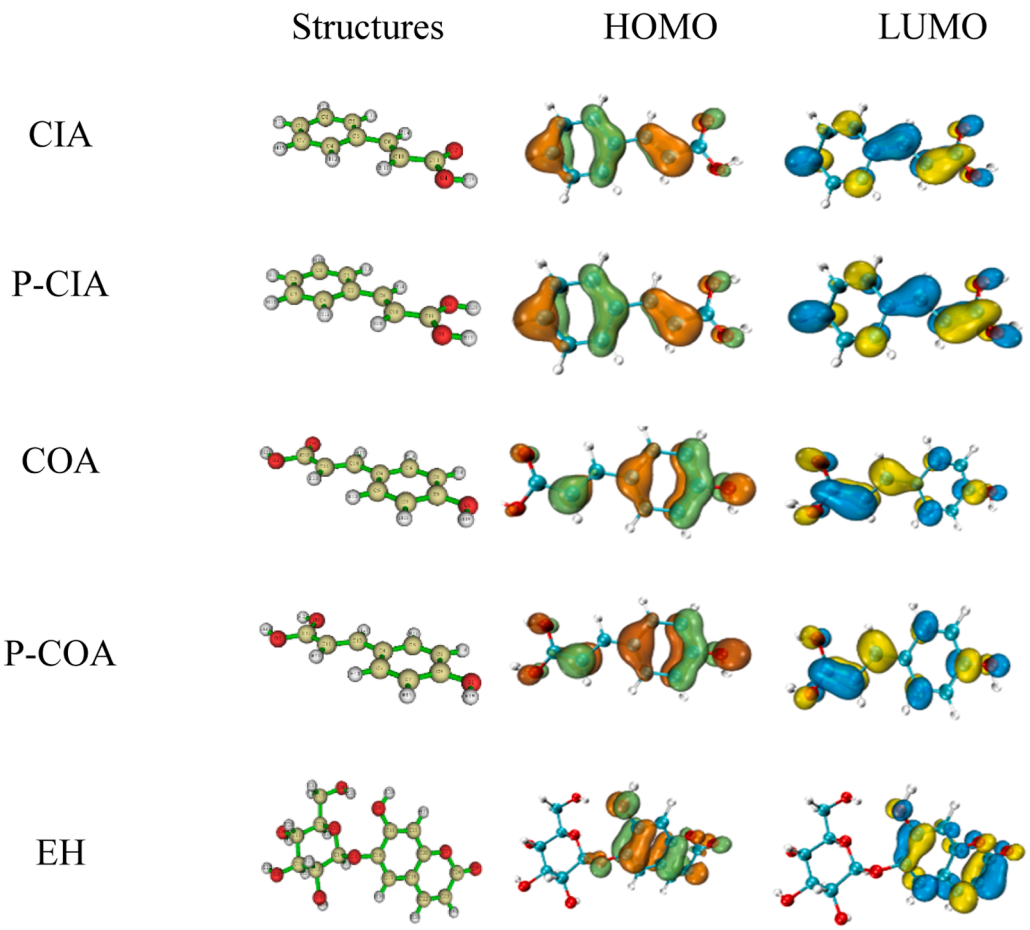


**Fig. 12.** Energy-Minimized Structures of Study Inhibitors in Neutral and Protonated Forms Using the B3LYP/6–31 G(d) Method.

**Table 8**
Global quantum chemical descriptors of organic corrosion inhibitors computed using DFT at the B3LYP/6–31 G (d) level.

| Descriptor | CIA | P-CIA | COA | P-COA | EH |
|---|---|---|---|---|---|
| $E_{HOMO}$ (eV) | -9.346 | -9.352 | -8.663 | -8.629 | -8.309 |
| $E_{LUMO}$ (eV) | -5.817 | -6.088 | -5.553 | -5.935 | -5.285 |
| $Gap_{(HOMO-LUMO)}$ (eV) | 3.53 | 3.264 | 3.11 | 2.694 | 3.023 |
| I (eV) | 9.346 | 9.352 | 8.663 | 8.629 | 8.309 |
| A (eV) | 5.817 | 6.088 | 5.553 | 5.935 | 5.285 |
| η (eV) | 1.765 | 1.632 | 1.555 | 1.347 | 1.512 |
| χ (eV) | 7.582 | 7.72 | 7.108 | 7.282 | 6.797 |
| σ (eV) | 0.567 | 0.613 | 0.643 | 0.742 | 0.661 |
| ω (eV) | 16.288 | 18.259 | 16.246 | 19.684 | 15.278 |
| $\Delta N_{Sn(001)} = \frac{4.42 - \chi_{inh}}{2\eta_{inh}}$ | -0,896 | -1011 | -0,864 | -1062 | -0,786 |
| $\Delta N_{SnO2(001)} = \frac{4.75 - \chi_{inh}}{2\eta_{inh}}$ | -0,802 | -0,910 | -0,758 | -0,940 | -0,677 |
| $\Delta N_{Fe(110)} = \frac{4.82 - \chi_{inh}}{2\eta_{inh}}$ | -0.782 | -0.889 | -0.736 | -0.914 | -0.654 |

adsorption behavior and interfacial interactions also depend on molecular orientation and surface characteristics, which are further examined through Fukui analysis and molecular dynamics simulations.

The corresponding ΔN values, obtained from Eq. (13) for Fe(110), Sn (001) and $SnO_2$(001) with the sign convention defined in Section 2.9, are also listed in Table 8.

### 3.7.2. Local reactivity analysis

*3.7.2.1. Fukui functions and electrostatic potential mapping.* To evaluate the reactivity of the studied organic corrosion inhibitors, we utilized Fukui functions and charge density distribution (CDD), which offer valuable insights into the local electronic properties of the molecules. Fukui functions quantify reactivity by examining changes in electron density upon electron addition or removal. At the same time, CDD highlights the redistribution of electron density when interacting with the metal surface or under different chemical conditions. The results of this analysis are presented in Table 9, where the Fukui indices ($f^-$, $f^+$) and CDD for each inhibitor are listed.

The electrostatic potential surface maps in Fig. 13 further illustrate the electron distribution across these molecules, helping identify the key reactive sites likely to interact with the metal surface in terms of electron donation and acceptance.

**Table 9**
Fukui indices ($f^-$, $f^+$), charge density differences (CDD), and main reactivity of the studied molecules.

| Molecule | Atom | $f^-$ | $f^+$ | CDD |
|---|---|---|---|---|
| CIA | 2(O) | 0.082 | 0.091 | 0.010 |
| | 6(C) | 0.058 | 0.099 | 0.041 |
| | 9(C) | 0.107 | 0.087 | -0.020 |
| | 10(C) | 0.128 | 0.095 | -0.033 |
| P-CIA | 2(O) | -0.0455 | -0.0667 | -0.0212 |
| | 6(C) | -0.1210 | -0.1248 | -0.0038 |
| | 9(C) | -0.0909 | -0.0792 | 0.0117 |
| | 11(C) | -0.1037 | -0.1199 | -0.0161 |
| COA | 3(O) | 0.0703 | 0.0917 | 0.0214 |
| | 9(C) | 0.0750 | 0.0705 | -0.0045 |
| | 10(C) | 0.0408 | 0.0720 | 0.0624 |
| | 12(C) | 0.1142 | 0.0930 | -0.0212 |
| P-COA | 1(O) | 0.0499 | -0.0625 | -0.1124 |
| | 2(O) | 0.0805 | -0.0727 | -0.1532 |
| | 3(O) | -0.0430 | -0.0589 | -0.0159 |
| | 10(C) | -0.0691 | 0.0481 | -0.0422 |
| | 12(C) | -0.2747 | -0.1071 | 0.1676 |
| EH | 2(O) | 0.0805 | -0.0727 | -0.1532 |
| | 8(O) | 0.0661 | 0.0503 | -0.0158 |
| | 18(C) | 0.0840 | 0.0152 | 0.1386 |
| | 22(C) | -0.0104 | -0.1206 | 0.0239 |
| | 23(C) | -0.0535 | -0.1547 | 0.0241 |

For CIA, the oxygen atom O2 exhibits comparable values of $f^-$(0.082) and $f^+$ (0.091), which identifies it as a dual reactive site, able both to donate electron density to the vacant orbitals of the metal and to accept electron density from them. The largest $f^-$ values, which characterise the electron-donating (nucleophilic) centres, are located on the vinylic and aromatic carbons C10 (0.128) and C9 (0.107), indicating that the conjugated system constitutes the principal donating region of the molecule. The CDD values, which show electron accumulation at the oxygen and carbon sites, are consistent with this description.

The ESP map highlights the negative potential around the oxygen atom, further confirming its nucleophilic character. In contrast, the protonated form, P-CIA, exhibits a modified local electronic distribution, with a decrease in electron density around key active centers, as indicated by the CDD and ESP maps, which may influence its interaction behavior with the metallic surface.

For COA, a similar behaviour is observed: O3 is again a dual site ($f^- = 0.0703$, $f^+ = 0.0917$), the strongest electron-donating character being found on C12 ($f^- = 0.1142$). At the same time, the CDD values indicate electron accumulation at the oxygen positions O3 and O10, which favours adsorption onto the metal surface. The ESP map also highlights these electron-rich regions. In P-COA, protonation attenuates the local reactivity of the oxygenated centres, as reflected in the depleted CDD values and in the ESP map, which shows a reduced electron density around the oxygen atoms. It should be noted that several condensed Fukui indices of the protonated species take negative values (Table 9). Negative condensed Fukui functions have no direct physical meaning and are a well-documented artefact of the finite-difference scheme combined with a Mulliken-type population analysis, to which charged and strongly polarised systems are particularly prone; these values are therefore used here in a qualitative sense only, and the description of the protonated forms relies primarily on the CDD and ESP maps. Finally, EH exhibits moderate reactivity, with balanced Fukui indices and slight electron accumulation at the oxygen atoms. The ESP map supports these findings, showing that the oxygen atoms are electron-rich but to a lesser extent compared to CIA and COA, suggesting potential but weaker interaction with the metal. In summary, the analysis of Fukui indices, CDD, and ESP maps (Fig. 13) reveals that neutral forms of CIA and COA exhibit strong reactivity, particularly at oxygen atoms, which makes them effective in metal surface interactions. However, protonation alters the distribution of electron density and the localization of reactive sites within the molecular framework, as observed in P-CIA and P-COA, demonstrating how protonation influences their interaction behavior as corrosion inhibitors.

## 3.8. Behavior of inhibitors on metal surfaces

To complement the local reactivity analysis, molecular dynamics (MD) simulations were performed to investigate the adsorption behavior of the studied inhibitors at different metal/solution interfaces. Particular attention was given to the Fe(110) surface due to its higher reactivity and its critical role in corrosion processes occurring at coating defects in tinplate systems. Adsorption geometries, radial distribution functions (RDF), and adsorption distances were analyzed to provide molecular-level insight into inhibitor–surface interactions and adsorption stability.

### 3.8.1. Molecular dynamics simulations

Fig. 14 illustrates the Molecular Dynamics Simulations of the adsorption geometries for the studied inhibitors on the Fe(110) surface, showing both their natural and protonated forms. The top row depicts the natural forms of CIA, COA, and EH, with the respective adsorption distances (AD) of 2.49 Å, 3.31 Å, and 2.97 Å, indicating the strength of their interaction with the metal surface. The bottom row shows the protonated forms (P-CIA and P- COA), with AD values of 3.25 Å and 3.03 Å, reflecting slightly weaker interactions compared to their neutral counterparts. The simulations highlight the structural arrangement of each inhibitor molecule in relation to the metal surface. In the natural

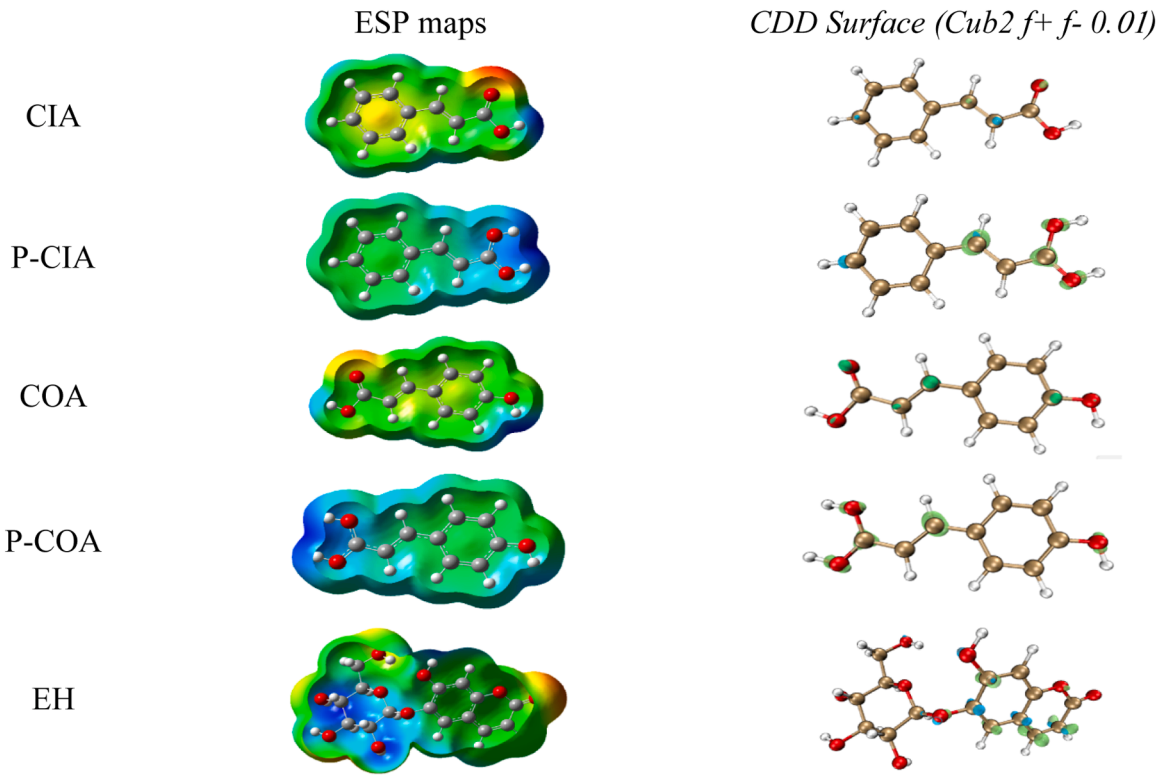


**Fig. 13.** Surface maps of electrostatic potential and charge density distributions for study inhibitors.

forms, the inhibitors are positioned closer to the surface, suggesting stronger binding, while in the protonated forms, the inhibitors exhibit slightly increased distances from the surface, indicating reduced interaction strength due to protonation.

### 3.8.2. Radial distribution function (RDF)

Table 10 presents the Radial Distribution Function (RDF) and adsorption distances (AD) for the studied inhibitors on the Fe(110) surface. The upper part of Fig. 15 shows the RDF, which illustrates how the inhibitors are distributed around the metal surface at varying distances. Peaks in the RDF curve represent preferred adsorption sites, with CIA showing a sharp peak at 2.49 Å, indicating strong and stable adsorption. In contrast, the RDF for P-CIA and P-COA is broader, suggesting weaker interactions with the surface after protonation. COA and EH exhibit intermediate RDF peaks, reflecting moderate adsorption strengths. The lower part of Fig. 15 compares the AD for each inhibitor, providing a quantitative measure of their interaction strength with the Fe(110) surface. CIA has the shortest adsorption distance of 2.49 Å, indicating a strong interaction, while P-CIA and P-COA exhibit longer distances (3.25 Å and 3.03 Å, respectively), reflecting weaker binding due to protonation. COA and EH show intermediate adsorption distances (3.31 Å and 2.97 Å, respectively), suggesting moderate interactions with the surface.

Together, these results indicate that neutral inhibitors like CIA and COA exhibit stronger interactions with the Fe(110) surface, while protonation weakens these interactions, as seen in P-CIA and P-COA. The RDF and adsorption distance data provide complementary insights into how the inhibitors interact with the surface at both the atomic and molecular levels.

## 3.9. Comparative analysis: multi-surface adsorption behavior

### 3.9.1. Adsorption distance comparison across metal surfaces

To comprehensively evaluate the protective capability of the studied inhibitors, their adsorption behavior was compared across three metallic surfaces: Sn(001), $SnO_2$(001), and Fe(110). Table 11 summarizes the key adsorption parameters obtained from molecular dynamics simulations, revealing striking differences in interaction strength.

The data reveal a clear hierarchy of adsorption strength: Fe(110) > > $SnO_2$(001) > Sn(001). The shortest adsorption distances, observed on Fe (110) (2.49–3.31 Å), correspond to a close-contact, flat-lying configuration in which the oxygenated functional groups are directly oriented towards the surface, whereas the markedly longer distances on Sn(001) (4.57–7.41 Å) and $SnO_2$(001) (3.77–6.80 Å) indicate a weak, essentially physical adsorption in which the molecules retain their solvation shell. This weaker adsorption behavior on Sn(001) and $SnO_2$(001) is further supported by the adsorption geometries and RDF profiles presented in the Supporting Information (Figs. S1–S3). This pronounced difference can be related to the higher work function of iron (Φ Fe(110) = 4.82 eV) compared with the tin surfaces (Φ $SnO_2$(001) = 4.75 eV and Φ Sn(001) = 4.42 eV). The significantly shorter approach observed on Fe(110) allows a much more effective overlap between the oxygenated groups and the surface. Since the force field employed here is non-reactive, these simulations describe the preferred adsorption geometry, the molecular orientation and the relative interaction strength on the three surfaces. In contrast, the coordinative character of the interaction at the exposed iron surface is supported by the localisation of the HOMO and of the Fukui $f^-$ indices on the oxygen atoms (Section 3.8). Examination of atomic-level interactions confirms that oxygen atoms, which carry the highest electron density as confirmed by Fukui indices and ESP maps, achieve optimal coordination geometry only on Fe(110) with O-metal distances of 2.47–3.43 Å. In contrast, weaker interactions are observed on $SnO_2$(001) (3.03–4.13 Å) and Sn(001) (3.09–3.83 Å), explaining the superior protective performance on the iron substrate.

### 3.9.2. Implications for tinplate corrosion protection

These comparative results provide important insights into the practical performance of the studied inhibitors in tinplate systems. On intact Sn/$SnO_2$ surfaces, the inhibitors exhibit weak physisorption (RDF > 3.7 Å) (Tables S1, Supporting Information), suggesting limited

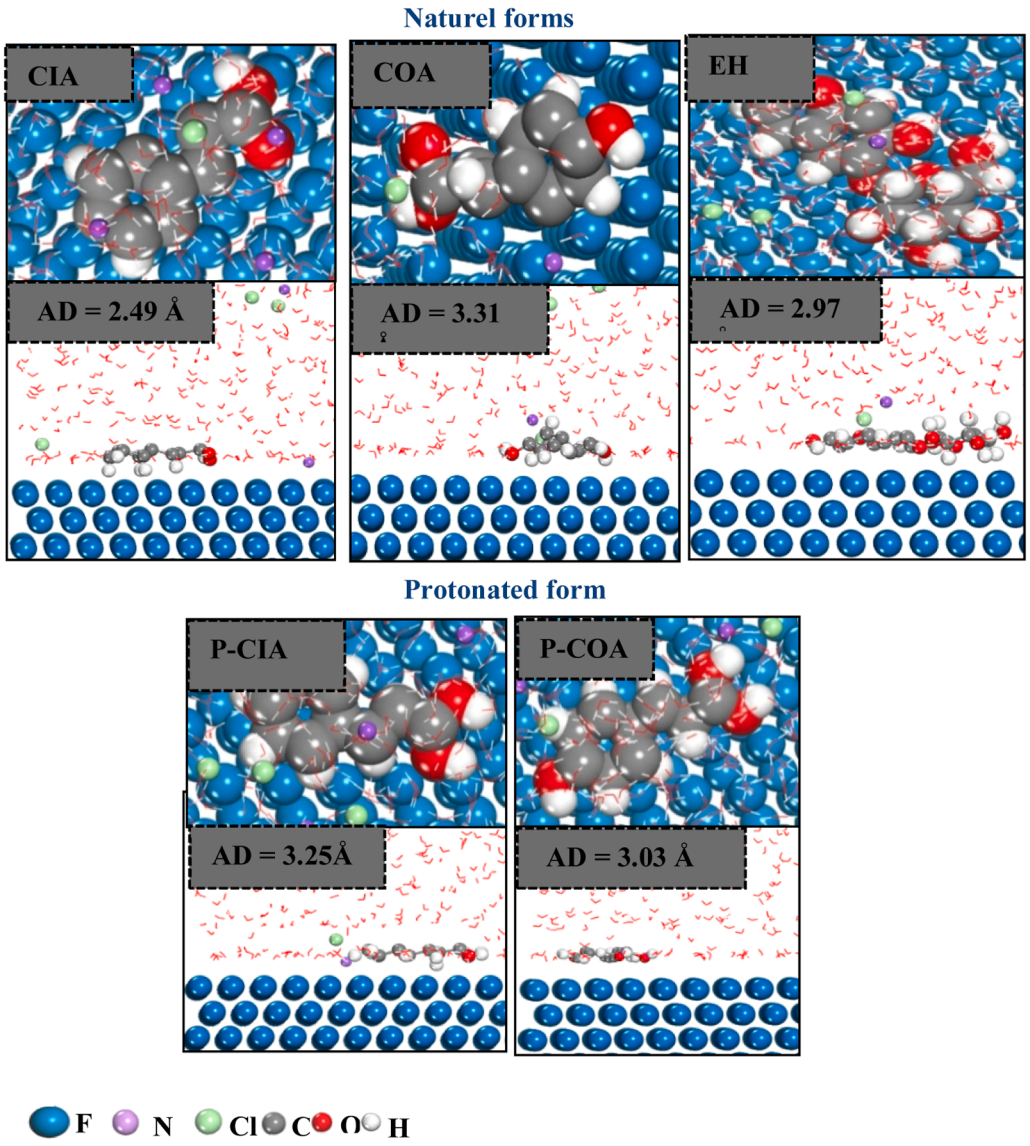


**Fig. 14.** Molecular dynamics simulations of adsorption geometries for the studied inhibitors on Fe (110) surface.

**Table 10**
Atomic Pair Adsorption Distances in (Å) for Active Atoms of the Studied Inhibitors on Fe (110) Surface.

| Atomic pair | CIA | P-CIA | COA | P-COA | EH |
|---|---|---|---|---|---|
| Fe | Adsorption Distances (AD) | | | | |
| Fe_1(O) | 3.15 | 2.47 | 2.83 | 3.43 | - |
| Fe_2(O) | 3.21 | 4.71 | 2.47 | 3.15 | 2.87 |
| Fe_3(O) | - | - | 2.51 | 2.49 | - |
| Fe _6(C) | 3.35 | 3.09 | - | - | - |
| Fe_8(O) | - | - | - | - | 2.51 |
| Fe_9(C) | - | - | 2.55 | 2.49 | - |
| Fe _10(C) | 3.35 | 3.35 | 2.51 | 2.51 | - |
| Fe _11(C) | 3.89 | 3.85 | - | - | - |
| Fe _12(C) | - | - | 3.49 | 2.39 | - |
| Fe _18(C) | - | - | - | - | 3.01 |
| Fe _22(C) | - | - | - | - | 2.55 |
| Fe _23(C) | - | - | - | - | 2.49 |
| RDF adsorption distance | 2.49 | 3.25 | 3.31 | 3.03 | 2.97 |

protective capability for the tin coating. However, once coating defects expose the underlying iron substrate, the inhibitors demonstrate a markedly enhanced adsorption on Fe(110) (2.49–3.31 Å), creating a stable protective film. This surface-dependent behavior indicates that the primary protective mechanism operates at the iron substrate level, where protection is most critically needed. At the same time, the weaker interactions with tin surfaces provide supplementary coverage on intact coating areas.

### 3.9.3. *Structure-activity relationships across surfaces*

The ranking of inhibitor effectiveness varies considerably with substrate type. The neutral forms (CIA, COA, EH) consistently demonstrate stronger adsorption on Fe(110) compared to their protonated counterparts, aligning with the detailed Fukui and ESP analysis presented earlier. However, on tin surfaces, the protonated forms sometimes exhibit shorter adsorption distances (e.g., P-CIA on both Sn and $SnO_2$), suggesting different adsorption mechanisms on oxide versus metallic iron surfaces. This surface-dependent behavior underscores the importance of evaluating corrosion inhibitors on the actual substrate requiring protection, as the iron substrate represents the critical surface that determines long-term corrosion resistance in tinplate systems.

The combined experimental–computational strategy adopted here is in line with the approach that has become established in recent studies of plant-derived inhibitors, in which gravimetric and electrochemical data are systematically correlated with quantum-chemical descriptors, molecular-dynamics adsorption configurations and direct surface

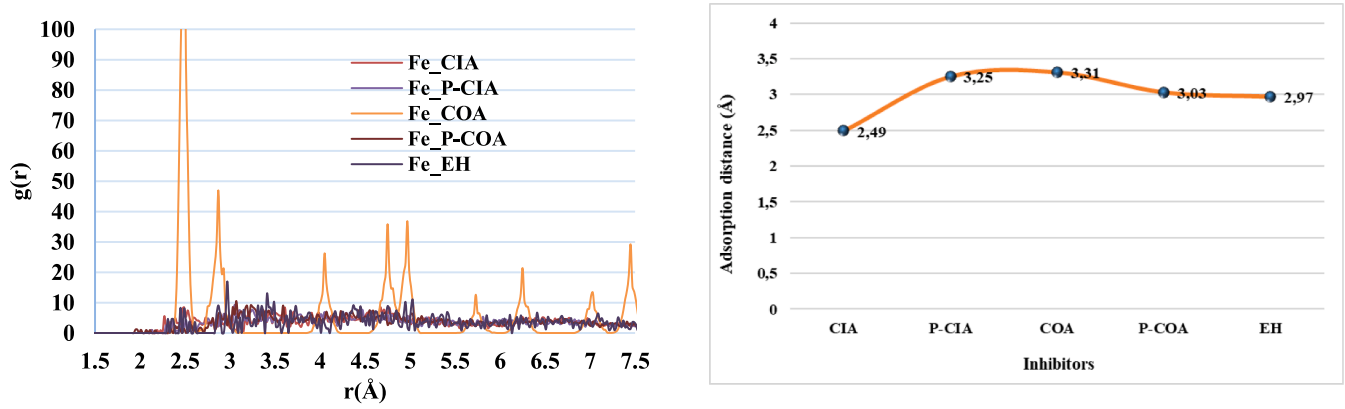


**Fig. 15.** Radial Distribution Function and Adsorption Distances of Inhibitors on Fe (110) Surface.

**Table 11**
Comparative Radial Distribution Function (RDF) Adsorption Distances (Å) on Different Metal Surfaces.

| Inhibitor | Sn(001) | $SnO_2$(001) | Fe(110) | Interaction Trend |
|---|---|---|---|---|
| CIA | 5.73 | 4.60 | 2.49 | Fe > > $SnO_2$ > Sn |
| P-CIA | 4.57 | 3.77 | 3.25 | Fe > $SnO_2$ > Sn |
| COA | 5.77 | 6.35 | 3.31 | Fe > > Sn ≈ $SnO_2$ |
| P-COA | 5.71 | 6.35 | 3.03 | Fe > > Sn ≈ $SnO_2$ |
| EH | 7.41 | 6.80 | 2.97 | Fe > > $SnO_2$ > Sn |

evidence, as reported for Nyctanthes arbor-tristis [57] and Calotropis gigantea [58] extracts on zinc in hydrochloric acid, for Ipomoea carnea leaf extract on aluminium [59], and for Millettia pinnata leaf extract on zinc [60]. The present work extends this approach in one respect that is specific to tinplate: because the substrate is heterogeneous, the adsorption behaviour was evaluated not on a single surface but comparatively on Fe(110), Sn(001) and $SnO_2$(001), which allows the protective action to be assigned specifically to the iron areas exposed at coating defects rather than to the intact tin coating.

### *3.10. Proposed mechanism of corrosion inhibition*

Based on the integrated experimental and computational evidence, the following corrosion inhibition mechanism is proposed for tinplate in the simulated black olive brine (SBOB) medium (41 g $L^{-1}$ NaCl + acetic acid, pH 4). BPE constituent molecules (CIA, COA, EH, and their protonated forms) adsorb spontaneously onto the tinplate surface, forming a protective interfacial layer. On the intact Sn/$SnO_2$ coating, the inhibitors mainly exhibit weak physisorption (adsorption distances = 3.77–7.41 Å), providing supplementary surface coverage. However, at coating defects where the underlying metallic substrate becomes accessible, the adsorption strength increases significantly, leading to the formation of a more stable protective film characterized by shorter adsorption distances (adsorption distances = 2.49–3.31 Å). Several interactions contribute to this adsorption process: (i) the interaction of the oxygen-containing functional groups, identified as the principal reactive centres by the Fukui $f^-$ indices and the ESP maps, with the metallic surface; (ii) the participation of the conjugated π system, consistent with the flat-lying adsorption geometries obtained from the simulations; and (iii) electrostatic anchoring involving the polar functional groups. The adsorbed inhibitor layer acts as a physical barrier that blocks both anodic and cathodic active sites, resulting in increased Rct and Rp values measured by EIS. At the same time, the gradual densification of the protective film explains the observed stabilization of the OCP with immersion time.

Consistently, CIA, which is the major identified constituent of the extract, exhibits the shortest adsorption distance on Fe(110) (2.49 Å), in agreement with the pronounced protective effect observed experimentally at the optimal concentration.

## 4. Conclusion

This work demonstrates that beet peel extract, an abundant agro-industrial byproduct, represents a highly effective and sustainable corrosion inhibitor for tinplate exposed to simulated black olive brine solution. The integration of gravimetric measurements, electrochemical techniques, surface characterization, and molecular simulations provided a comprehensive understanding of the inhibition mechanism from both macroscopic and molecular perspectives. The extract achieved maximum inhibition efficiencies of 99.38% (EIS) and 94.8% (weight loss) at 300 mg $L^{-1}$ , confirming the formation of a compact and stable protective film that effectively suppressed both anodic and cathodic corrosion reactions.

Surface analyses (SEM-EDX and FTIR) demonstrated the adsorption of bioactive polyphenolic constituents onto the tinplate surface. In contrast, adsorption thermodynamics revealed a spontaneous Langmuir-type adsorption process of mixed character, consistent with the surface-dependent behaviour identified computationally: predominantly physical on the intact Sn/$SnO_2$ coating, with a stronger, coordinative contribution once the underlying iron substrate becomes accessible at coating defects. Theoretical investigations further supported the experimental observations by identifying oxygen-containing functional groups as the primary adsorption sites. Comparative molecular dynamics simulations showed that adsorption is considerably stronger on Fe(110) than on intact Sn(001) and $SnO_2$(001) surfaces, providing new insight into the preferential protection of exposed steel regions generated by coating defects or localized degradation.

Beyond its excellent anticorrosion performance, this study highlights the environmental value of converting beet-processing waste into a high-value corrosion inhibitor, contributing simultaneously to waste valorization, circular economy principles, and the replacement of conventional toxic inhibitors. The proposed integrated experimental and computational methodology also provides a robust framework for designing next-generation bio-based corrosion inhibitors for food-packaging systems and other environmentally sensitive industrial applications. Future investigations should focus on long-term durability, real food-storage environments, and scale-up assessment to facilitate industrial implementation.

## CRediT authorship contribution statement

**Amel Serhane:** Writing – original draft, Visualization, Validation, Methodology, Investigation, Formal analysis, Data curation, Conceptualization. **Yamina Boudinar:** Writing – original draft, Visualization, Validation, Methodology, Investigation, Formal analysis, Data curation,

Conceptualization. **Hakim Bensabra:** Visualization, Validation, Methodology, Investigation, Formal analysis, Data curation, Conceptualization. **Noura Naili:** Visualization, Validation, Methodology, Investigation, Formal analysis, Data curation, Conceptualization. **Amina Benaissa:** Visualization, Validation, Investigation, Formal analysis. **Sihem Boufas:** Writing – original draft, Visualization, Validation, Investigation, Formal analysis, Data curation, Conceptualization. **Abdul Ahad:** Writing – review & editing, Visualization, Validation. **Hyun-Jo Ahn:** Writing – review & editing, Visualization, Validation, Investigation. **Byong-Hun Jeon:** Writing – review & editing, Visualization, Validation, Resources, Investigation, Funding acquisition. **Yacine Benguerba:** Writing – review & editing, Visualization, Validation, Supervision, Project administration, Methodology.

## Supplementary material

Supplementary data associated with this article are provided as a separate Supporting Information file, comprising Figs. S1-S3 (adsorption geometries and radial distribution functions of the studied inhibitors on the Sn(001) and $SnO_2$(001) surfaces) and Table S1 (the corresponding atomic-pair adsorption distances).

## Declaration of Competing Interest

The authors declare that they have no known competing financial interests or personal relationships that could have appeared to influence the work reported in this paper.

## Acknowledgments

The authors are grateful to the High-Performance Computing (HPC) resources of UCI-UFMC (Unité de Calcul Intensif of the University Fréres Mentouri Constantine 1), Algeria, Laboratory of Applied Energetics and Materials (LEAM), University of Jijel, Algeria, and Laboratory of anti-corrosion materials environment and structure, 20 Août 1955 University, Skikda, Algeria, for the provision of research facilities for this work. They also acknowledge the Mid-Career Research Program (Grant No. RS-2025-00520940) of the Ministry of Education and the Government of the Republic of Korea. The authors further extend their sincere appreciation to the Ongoing Research Funding Program (ORF-2026-959), King Saud University, Riyadh, Saudi Arabia.

## Appendix A. Supporting information

Supplementary data associated with this article can be found in the online version at doi:10.1016/j.mtcomm.2026.116428.

## Data availability

No data was used for the research described in the article.

## References

[1] L. Pagnotta, Metal packaging: from monolithic containers to hybrid architectures, Materials 19 (6) (2026) 1177.
[2] J.N. Pejić, B.V. Jegdić, B.M. Radojković, A.R. Simović, A.S. Popović, S.G. Eraković Pantović, D.D. Marunkić, Causes of occurrence and methods of prevention of corrosion of cans for food products, Russ. J. Electrochem. 61 (8) (2025) 446–458.
[3] Y. Wu, K. Ruffley, M.A. Pascall, Investigation and mechanism of headspace corrosion in metal cans filled chicken noodle soup, Packag. Technol. Sci. 37 (3) (2024) 187–197.
[4] A. Ansari, Y.S. Siddiqui, M.A. Quraishi, Corrosion of tin can and its inhibition: a review, Int. J. Corros. Scale Inhib. 8 (4) (2019) 816–834, https://doi.org/10.17675/2305-6894-2019-8-4-3.
[5] J.R. Xavier, S.P. Vinodhini, A. Priyadharshini, Multifunctional epoxy-based nanocomposite coating for tinplate: enhancing food packaging with superior mechanical, anticorrosion, and antimicrobial properties, Int. J. Biol. Macromol. 309 (Part1) (2025) 142671.
[6] W. Daoudi, A. El Aatiaoui, O. Dagdag, K. Zaidi, R. Haldhar, S.-C. Kim, A. Oussaid, A. Aouinti, A. Berisha, F. Benhiba, E.E. Ebenso, A. Oussaid, Anticorrosion coating formation by a biopolymeric extract of Artemisia herba-alba plant: experimental and theoretical investigations, Coatings 13 (3) (2023) 611.
[7] H. Ahchouch, M. El House, A.H. Al-Moubaraki, E.A. Noor, A. Hadfi, A. Driouiche, L. Bammou, M. Belkhaouda, R. Salghi, M. Chafiq, A. Chaouiki, Y.G. Ko, From nature to protection: unleashing the protective potential of Hedera helix leaves against corrosion in harsh acidic environments using experimental and theoretical insights, Arab. J. Chem. 17 (2) (2024) 105593.
[8] A. Najem, O.S. Campos, G. Girst, M. Raji, A. Hunyadi, J. García-Antón, A. Bellaouchou, H.M.A. Amin, M. Boudalia, Experimental and DFT atomistic insights into the mechanism of corrosion protection of low-carbon steel in an acidic medium by polymethoxyflavones from Citrus peel waste, J. Electrochem. Soc. 170 (9) (2023) 093512.
[9] W.R. de Souza Morais, J.S. da Silva, N.M.P. Queiroz, C.L. de Paiva e Silva Zanta, A. S. Ribeiro, J. Tonholo, Green corrosion inhibitors based on plant extracts for metals and alloys in corrosive environment: a technological and scientific prospection, Appl. Sci. 13 (13) (2023) 7482.
[10] P. Shathani, E.N. Ogunmuyiwa, B.A. Obadele, O.P. Oladijo, Plant leaf extracts as green corrosion inhibitors of steel in acidic and seawater environments: a review, Environ. Sci. Pollut. Res. (2025) 1–22.
[11] L. Adlani, N. Benzbiria, A.T. Iti, N. Timoudan, I. Warad, AlObaid, A. Zarrouk, Adsorption and inhibition mechanisms of new pyrazole derivatives for carbon steel corrosion in hydrochloric acid solutions based on experimental, computational, and theoretical calculations, ACS Omega 9 (12) (2024) 13746–13763.
[12] H. Boughazi, Y. Boudinar, S. Tlili, A. Djedouani, N. Naili, Electrochemical, surface, DFT, and ADMET insights into (*E*)-2-(2-hydroxybenzylidene) hydrazine-1-carboxamide as a corrosion inhibitor, RSC Adv. 15 (46) (2025) 38946–38968.
[13] N. Naili, A. Benaïssa, F. Chekkal, M.A. Zerizer, B. Zouchoune, A. Bouhadiba, N. Redjem, DFT prediction of Dichlorvos β-cyclodextrin inclusion complex: energetic and non-covalent interaction insights, Struct. Chem. 36 (2) (2025) 527–541.
[14] I.B. Obot, D.D. Macdonald, Z.M. Gasem, Density Functional Theory (DFT) modeling and Monte Carlo simulation studies on the inhibition of mild steel corrosion by triazoles, J. Mol. Graph. Model. 70 (2016) 241–254.
[15] F. Ennafaa, A. Chraka, K. Tassaoui, I. Mouamr, M. Damej, A.E.L. Mahmoudi, M. Benmessaoud, An experimental and dual computational study using DFT and MD simulations to better understand the adsorption and corrosion-inhibiting properties of N-(3-(4-Methoxyphenyl) isoxazol-5-yl) methyl saccharin for C38 Steel in acidic medium, Mater. Chem. Phys. 334 (2025) 130441.
[16] R.G. Parr, W. Yang, Density-Functional Theory of Atoms and Molecules, Oxford University Press, Oxford, UK, 1984.
[17] A.O. Alaoui, W. Elfalleh, B. Hammouti, A. Titi, M. Messali, S. Kaya, F. El-Hajjaji, Theoretical prediction of corrosion inhibition by ionic liquid derivatives: a DFT and molecular dynamics approach, R. Soc. Chem. 15 (16) (2025) 12645–12652.
[18] P. Ainsworth, Ş. İbanoğlu, A. Plunkett, E. İbanoğlu, V. Stojceska, Effect of brewers' spent grain addition and screw speed on the selected physical and nutritional properties of an extruded snack, J. Food Eng. 81 (4) (2007) 702–709.
[19] A. Arvouet-Grand, B. Vennat, A. Pourrat, P.J. Legret, Standardization of propolis extract and identification of principal constituents, J. De. Pharm. De. Belg. 49 (6) (1994) 462–468.
[20] A.D. Becke, Density-functional thermochemistry. III. The role of exact exchange, J. Chem. Phys. 98 (7) (1993) 5648–5652.
[21] V. Barone, M. Cossi, Quantum Calculation of Molecular Energies and Energy Gradients in Solution by a Conductor Solvent Model, J. Phys. Chem. A 102 (11) (1998) 1995–2001.
[22] Y. Takano, K.N. Houk, Comparative analysis of the conductor-type polarizable continuum model (CPCM) for aqueous solvation-free energies of neutral and ionic organic molecules, J. Chem. Theory Comput. 1 (1) (2005) 70–77.
[23] Gaussian 09, A.1 Revision, M.J. Frisch, G.W. Trucks, H.B. Schlegel, G.E. Scuseria, M.A. Robb, J.R. Cheeseman, G. Scalmani, V. Barone, B. Mennucci, G.A. Petersson, H. Nakatsuji, M. Caricato, X. Li, H.P. Hratchian, A.F. Izmaylov, J. Bloino, G. Zheng, J.L. Sonnenberg, M. Hada, M. Ehara, K. Toyota, R. Fukuda, J. Hasegawa, M. Ishida, T. Nakajima, Y. Honda, O. Kitao, H. Nakai, T. Vreven, J.A. Montgomery Jr., J. E. Peralta, F. Ogliaro, M. Bearpark, J.J. Heyd, E. Brothers, K.N. Kudin, V. N. Staroverov, R. Kobayashi, J. Normand, K. Raghavachari, A. Rendell, J.C. Burant, S.S. Iyengar, J. Tomasi, M. Cossi, N. Rega, J.M. Millam, M. Klene, J.E. Knox, J. B. Cross, V. Bakken, C. Adamo, J. Jaramillo, R. Gomperts, R.E. Stratmann, O. Yazyev, A.J. Austin, R. Cammi, C. Pomelli, J.W. Ochterski, R.L. Martin, K. Morokuma, V.G. Zakrzewski, G.A. Voth, P. Salvador, J.J. Dannenberg, S. Dapprich, A.D. Daniels, Ö. Farkas, J.B. Foresman, J.V. Ortiz, J. Cioslowski, D. J. Fox, Gaussian 09, Revision A.1, 121, Gaussian, Inc., Wallingford, CT, USA, 2009, pp. 150–166.
[24] R.G. Parr, L.V. Szentpály, S. Liu, Electrophilicity index, J. Am. Chem. Soc. 121 (9) (1999) 1922–1924.
[25] D. Zouied, A. Benaissa, N. Bouzenad, M. Khelfaoui, I. Boussouf, R.N. Boucetta, E. Can, A. Titah, N. Naili, K. Bekouche, R. Selaimia, S. Boucetta, Integrated biosorption of crystal violet using raw and cellulose-extracted Cucurbita pepo L. peels: experimental study coupled with DFT, NCI-RDG, and molecular dynamics simulations, Chem. Pap. (2026) 1–18.
[26] A. Benaissa, A. Bouhadiba, N. Naili, F. Chekkal, M. Khelfaoui, I. Bouras, F. Madi, Computational investigation of dimethoate and β-cyclodextrin inclusion complex: molecular structures, intermolecular interactions, and electronic analysis, Struct. Chem. 34 (3) (2023) 1189–1204.
[27] F. Chekkal, N. Naili, A. Benaissa, M.A. Zerizer, B. Zouchoune, N. Redjem, A proposed process for trichlorfon and β-cyclodextrin inclusion complexation by DFT investigation, Struct. Chem. 35 (5) (2024) 1539–1549.

[28] M.Esmaeilzadeh Khabazi, A.Najafi Chermahini, DFT study on corrosion inhibition by tetrazole derivatives: investigation of the substitution effect, ACS Omega 8 (11) (2023) 9978–9994.
[29] A.O. Alaoui, W. Elfalleh, B. Hammouti, A. Titi, M. Messali, S. Kaya, F. El-Hajjaji, Theoretical prediction of corrosion inhibition by ionic liquid derivatives: a DFT and molecular dynamics approach, RSC Adv. 15 (16) (2025) 12645–12652.
[30] W. Yang, W.J. Mortier, The use of global and local molecular parameters for the analysis of the gas-phase basicity and proton affinity of amines, J. Am. Chem. Soc. 108 (19) (1986) 5708–5711.
[31] M. Khelfaoui, A. Benaissa, D. Zouied, N. Naili, Y. Belhocine, N. Boucetta, F. Chekkal, M. Rouainia, B. Zouchoune, Eco-friendly corrosion inhibition of C1020 carbon steel in 1 M HCl by *Cytisus villosus* leaf extract: combined electrochemical, surface, and molecular-level insights, *Chem. Pap. * (2026) 1–23.
[32] Politzer, P., & Murray, J.S., The fundamental nature and role of the electrostatic potential in atoms and molecules. Theoretical Chemistry Accounts, 12002. 08(3), 134-142.
[33] BIOVIA, Dassault Systèmes, Materials Studio, Version 2023, Dassault Systèmes, San Diego, 2023.
[34] F. Chen, X. Zhang, J. Wang, F. Wang, J. Mao, P-coumaric acid: advances in pharmacological research based on oxidative stress, Curr. Top. Med. Chem. 24 (5) (2024) 416–436.
[35] S. Ju, Y. Tan, Q. Wang, L. Zhou, K. Wang, C. Wen, M. Wang, Antioxidant and anti-inflammatory effects of esculin and esculetin, Exp. Ther. Med. 27 (6) (2024) 1–14.
[36] D. Veys-Renaux, S. Reguer, L. Bellot-Gurlet, F. Mirambet, E. Rocca, Conversion of steel by polyphenolic model molecules: corrosion inhibition mechanism by rutin, esculin, esculetol, Corros. Sci. 136 (2018) 1–8.
[37] A. Singh, E.E. Ebenso, M. Quraishi, Corrosion inhibition of carbon steel in HCl solution by some plant extracts, Int. J. Corros. 2012 (1) (2012) 897430.
[38] S. Deng, X. Li, Inhibition by Ginkgo leaves extract of the corrosion of steel in HCl and H2SO4 solutions, Corros. Sci. 55 (2012) 407–415.
[39] P.B. Raja, P.B, M.G. Sethuraman, Natural products as corrosion inhibitor for metals in corrosive media—a review, Mater. Lett. 62 (1) (2008) 113–116.
[40] A. El-Etre, Inhibition of acid corrosion of carbon steel using aqueous extract of olive leaves, J. Colloid Interface Sci. 314 (2) (2007) 578–583.
[41] M.K. Pavithra, T.V. Venkatesha, K. Vathsala, K.O. Nayana, Synergistic effect of halide ions on improving corrosion inhibition behaviour of benzisothiozole-3-piperizine hydrochloride on mild steel in 0.5 M H2SO4 medium, Corros. Sci. 52 (11) (2010) 3811–3819.
[42] A. Farhadian, A. Rahimi, N. Safaei, A. Shaabani, M. Abdouss, A. Alavi, A theoretical and experimental study of castor oil-based inhibitor for corrosion inhibition of mild steel in acidic medium at elevated temperatures, Corros. Sci. 175 (2020) 108871.
[43] M. Chadili, M.M. Rguiti, B. El Ibrahimi, R. Oukhrib, A. Jmiai, M. Beelkhaouda, L. Bammou, M. Hilali, L. Bazzi, Corrosion inhibition of 3003 aluminum alloy in molar hydrochloric acid solution by olive oil mill liquid byproduct, Int. J. Corros. 2021 (1) (2021) 6662395.
[44] B. Hamrahi, A. Khanlarkhani, S.M. Madani, A. Fattah-alhosseini, S.O. Gashti, Evaluation of henna extract performance on corrosion inhibition of API 5L steel in H2S-containing medium and DFT quantum computing of its constituents, Met. Mater. Int. 27 (11) (2021) 4463–4476.
[45] A. Boutoumit, M. Elhawary, A. Bellaouchou, M. Boudalia, O. Hammani, A. José Garcia, H.M. Amin, Electrochemical, structural, and thermodynamic investigations of methanolic parsley extract as a green corrosion inhibitor for C37 steel in HCl, Coatings 14 (7) (2024) 783.
[46] A. Acidi, A. Sedik, A. Rizi, R. Bouasla, K.O. Rachedi, M. Berredjem, A. Delimi, A. Abdennouri, Y. Bengureba, Examination of the main chemical components of essential oil of Syzygium aromaticum as a corrosion inhibitor on the mild steel in 0.5 M HCl medium, J. Mol. Liq. 391 (2023) 123423.
[47] A.S. Fouda, H.E. Megahed, N. Fouad, N.M. Elbahrawi, Corrosion inhibition of carbon steel in 1 M hydrochloric acid solution by aqueous extract of Thevetia peruviana, J. Bio- Tribo-Corros. 2 (3) (2016) 16.
[48] S. Umoren, Z. Gasem, I. Obot, Date palm (Phoenix dactylifera) leaf extract as an eco-friendly corrosion inhibitor for carbon steel in 1M hydrochloric acid solution, Anticorros. Methods Mater. 62 (1) (2015) 19–28.
[49] A.H. Alamri, I. Obot, Highly efficient corrosion inhibitor for C1020 carbon steel during acid cleaning in multistage flash (MSF) desalination plant, Desalination 470 (2019) 114100.
[50] Y. Zhou, C. Zhu, S. Xu, B. Xiang, R. Marzouki, Combining electrochemical, surface topography analysis, and theoretical calculation methods to insight into the anticorrosion property of Syzygium samarangense leaf extract, J. Ind. Eng. Chem. 102 (2021) 302–311.
[51] M.A. Abbas, E.I. Arafa, E.S. Gad, M.A. Bedair, O.E. El-Azabawy, H.I. Al-Shafey, Performance assessment by experimental and Theoretical approaches of newly synthesized benzyl amide derivatives as corrosion inhibitors for carbon steel in 1.0 M hydrochloric acid environment, Inorg. Chem. Commun. 143 (2022) 109758.
[52] H. Tristijanto, M.N. Ilman, P.T. Iswanto, Corrosion inhibition of welded of X–52 steel pipelines by sodium molybdate in 3.5% NaCl solution, Egypt. J. Pet. 29 (2) (2020) 155–162.
[53] A. Jmiai, M.T. Sfaira, A.El Hassane, M.Ebn Touhami, A. Srhiri, A. Jbara, Zizyphus lotus pulp (jujube extract) as a green and promising corrosion inhibitor for copper in acidic medium, J. Mol. Liq. 268 (2018) 102–113.
[54] M. Lebrini, M. Lagrenée, H. Vezin, M. Traisnel, F. Bentiss, Experimental and theoretical study for corrosion inhibition of mild steel in normal hydrochloric acid solution by some new macrocyclic polyether compounds, Corros. Sci. 49 (5) (2007) 2254–2269.
[55] R. Solmaz, Investigation of the inhibition effect of 5-((*E*)-4-phenylbuta-1, 3-dien-ylideneamino)-1, 3, 4-thiadiazole-2-thiol Schiff base on mild steel corrosion in hydrochloric acid, Corros. Sci. 52 (10) (2010) 3321–3330.
[56] M. Sabiha, Y. Kerroum, M. El Hawary, M. Boudalia, A. Bellaouchou, O. Hammani, H.M.A. Amin, Investigating the adsorption and corrosion protection efficacy and mechanism of marjoram extract on mild steel in HCl medium, Molecules 30 (2) (2025) 272, https://doi.org/10.3390/molecules30020272.
[57] B.B. Parmar, P.S. Desai, Sustainable zinc corrosion protection in acidic media via ethanolic Nyctanthes arbour-tristis leaf extract: a combined theoretical and experimental study, J. Bio- Tribo-Corros. 11 (4) (2025) 104.
[58] B.B. Parmar, P.S. Desai, Sustainable zinc corrosion control in hydrochloric acid using Calotropis gigantea: a multi-approach investigation combining experiments, RSM, and quantum simulations, Chem. Pap. 80 (2) (2026) 1665–1689.
[59] A.M. Patel, K.C. Desai, R.T. Vashi, P.S. Desai, Integrated experimental-theoretical analysis of aluminum corrosion inhibition by Ipomoea carnea leaf extract, Sustain. Chem. One World 9 (2026) 100182.
[60] B.B. Parmar, P.S. Desai, Integrated experimental and theoretical analysis of Millettia pinnata (Karanja) leaf extract as an eco-friendly inhibitor for zinc in hydrochloric acid, Materials 11 (2026) 101732.